crystals

MDPI

Review

Impurity-Tolerance Design and Strengthening–Toughening Strategies in Recycled Aluminium Alloys

Dongxu Yang [1,*], Huafeng Wei [1], Haozhe Li [1], Hongwu Zhang [1], Zengwu Yue [1] and Xingshuo Liu [2]

[1] Shandong Power Industry Boiler & Pressure Vessel Inspection Center Co., Ltd., Jinan 250022, China
[2] School of Materials Science and Engineering, University of Jinan, Jinan 250022, China
* Correspondence: sddkyydx@163.com

Abstract

Recycled aluminium moves from downcycling towards the automotive sheet, structural castings and high-performance extrusions. The central constraint on closed-loop recycling is no longer the mere presence of impurities. It is the multiscale microstructure that those impurities generate during solidification, heat treatment and deformation, and how that microstructure participates in load bearing and damage. Iron is the most representative cumulative impurity because its equilibrium solubility in solid aluminium is low and its removal by conventional refining is difficult and costly. At a given Fe content, variations in Si, Mn, Cu and Cr, cooling rate and downstream processing can produce plate-like β-Al-Fe-Si, Chinese-script α-Al(Fe,Mn)Si, $Al_6(Fe,Mn)$, $Al_{13}Fe_4$ and Al_7Cu_2Fe intermetallics with distinct size distributions, shape anisotropy, three-dimensional connectivity, phase fractions and interface states. Consequently, Fe content has no alloy-independent monotonic relationship with strength, ductility or damage tolerance. This review follows a composition-phase selection-three-dimensional microstructure-mechanical response evidence chain to examine Fe-rich intermetallic formation and evolution, strengthening-damage competition, alloying and solidification control, thermomechanical processing, solid-state recycling and coupled Fe-Si-Cu-Mn-Zn effects. The available evidence supports defining impurity tolerance as a microstructural acceptance window tied to the alloy system, processing route and target property, rather than as a fixed compositional ceiling. Its assessment must at least account for the hazardous upper tail of particle-size distribution, morphology, three-dimensional connectivity, phase fraction, matrix strength and interface integrity. CALPHAD, in situ synchrotron methods, three-dimensional X-ray computed tomography and machine learning are shifting recycled-alloy design from grade-based impurity limits towards composition-process feasibility domains matched to scrap distributions. Comparable three-dimensional descriptors, quantitative matrix-particle-damage maps and robust design methods for variable feedstocks are now required to complete this transition.

Keywords: recycled aluminium alloys; impurity tolerance; Fe-rich intermetallic compounds; three-dimensional connectivity; strengthening and toughening; damage; CALPHAD; machine learning

Check for updates

Academic Editor: Shouxun Ji

Received: 20 September 2026
Revised: 6 October 2026
Accepted: 9 October 2026
Published: 16 October 2026

Copyright: © 2026 by the authors. Licensee MDPI, Basel, Switzerland. This article is an open access article distributed under the terms and conditions of the Creative Commons Attribution (CC BY) license.

1. Introduction

The energy and carbon benefits of aluminium recycling are well established, but recycled material is not intrinsically high value [1–7]. Figure 1 translates this system-level advantage into a materials-design problem. Closed-loop processing retains material value through sorting, remelting and remanufacture, while impurities that are difficult to remove

accumulate over successive cycles (Figure 1a) [1,4–6,8–11]. The much lower embodied energy of secondary production establishes the direct environmental value of increasing scrap use (Figure 1b). The Fe-Mn-Si maps further show that impurity risk is not controlled by Fe alone, but shifts with companion elements and the targeted microstructural window (Figure 1c,d). In Figure 1d, f is the corrected fraction, defined as the phase fraction of script-like α phases divided by the total Fe-rich intermetallic phase fraction. Under the Scheil-Gulliver calculation used in Ref. [12], f = 1 indicates that the predicted Fe-rich fraction contains no platelet phase. As automotive body sheets, extrusions, battery trays and large integrated castings enter the end-of-life stream, scrap will increasingly change from compositionally uniform production offcuts to post-consumer mixtures containing multiple grades, joining technologies and surface conditions. Sorting can reduce this heterogeneity but cannot restore the narrow composition distributions associated with primary aluminium [5,6,10]. Fe, Cu, Si, Zn, Mn and Mg, therefore, become batch-dependent feedstock attributes that accumulate with repeated recycling rather than occasional specification excursions [1–3,5,6,8–11].

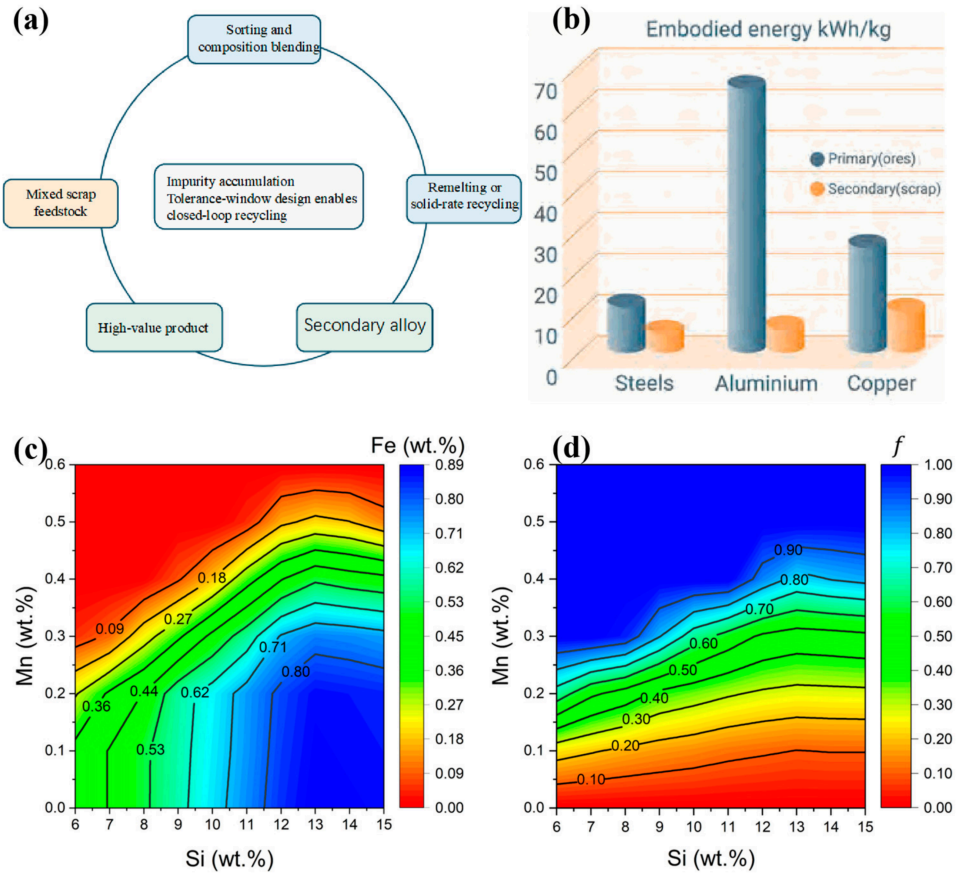


Figure 1. Why impurity-tolerance is required for high-value aluminium recycling. (**a**) Closed-loop pathway linking scrap sorting, recycling, secondary-alloy production and impurity accumulation. (**b**) Embodied-energy comparison between primary and secondary production. (**c**) Critical Fe content as a function of Si and Mn. (**d**) Corrected fraction f, defined as the fraction of script-like α phases within the total Fe-rich intermetallic phase fraction; f = 1 denotes complete suppression of the platelet fraction in the Scheil-Gulliver prediction. Panel (**a**) was redrawn; the remaining panels were adapted and recomposed from Refs. [1,12].

Iron is a good representative because two of its constraints act simultaneously. First, its equilibrium solubility in solid aluminium is very low, so it mainly occurs as Fe-rich intermetallic compounds under conventional casting conditions [8,9,13–17]. Second, its sep-

aration is constrained by thermodynamics, density contrast, particle size and process cost. Sedimentation, filtration, salt fluxes, centrifugation and intermediate-phase enrichment can reduce Fe in selected melts, but often require additional alloying, prolonged holding or dedicated equipment, and can cause metal loss and secondary dross [4,13,18–20]. Recycled aluminium therefore poses two distinct questions: purification asks how Fe can be removed, whereas tolerance design asks how the residual Fe can be organised and used safely. Conflating these questions reduces materials design to the unhelpful premise that purer is always better.

Conventional compositional limits remain useful engineering screens, but their meaning must be tied to a specific alloy, process and property. Fe sensitivity differs among 6xxx sheets and extrusion alloys, Al-Si cast alloys and high-strength 2xxx/7xxx alloys [8,9,16,17,21–23]. Even within one series, cooling history, homogenisation, strain, solution treatment, ageing and the spatial distribution of second phases can alter the response [16,23–33]. In recycled AA6016, intermediate Fe contents retained properties close to the low-Fe reference, whereas higher Fe promoted primary intermetallics, local network formation and reduced β″ precipitation, with corresponding losses in strength and ductility [34]. This result identifies a transition range for one AA6016 composition-process path, not a universal limit for all 6xxx alloys.

Recycled 6111 defines a different evidence boundary. Fully recycled IBA6111 contains a substantially greater number density and volume fraction of Fe-rich particles than commercial AA6111, yet it can retain useful strength and uniform elongation [23,35,36]. The principal divergence emerges after necking, when faster void growth and coalescence reduce total elongation and the remaining damage reserve [35–38]. High-resolution digital image correlation (HRDIC) and electron backscatter diffraction (EBSD) further show that a high particle density shifts local plasticity from predominantly grain-boundary-controlled deformation towards particle-neighbourhood localisation. Particle cracking probability is jointly controlled by morphology, orientation, spatial proximity and local strain [35,37,38]. Higher Fe therefore does not necessarily reduce strength and elongation in parallel, and mean tensile metrics alone cannot define damage tolerance.

These observations move the central question from whether Fe exceeds a limit to which Fe-rich microstructures remain acceptable. Figure 2 establishes the first link between phase selection and geometric risk. Figures 2a and 2b are equilibrium isopleths for Al-11Si-0.7Fe-xMn and Al-11Si-1.4Fe-xMn (wt.%), respectively [12]. The labelled composition intervals describe distinct formation scenarios. Zone c restricts platelet β and Chinese-script α_C phases to the final eutectic reaction. Zone d represents partial replacement of fine β platelets by larger pre-eutectic Chinese-script α_C. Zones e and f represent excessive Mn, which suppresses fine β platelets but promotes coarse polyhedral α_C particles. Under severe Fe contamination, zone g produces coarse pre-eutectic or primary β platelets; zone h introduces pre-eutectic Chinese-script α_C and reduces the coarse β fraction; zone i further reduces β size and fraction while promoting polyhedral and Chinese-script α_C; and zone j stabilises coarse primary polyhedral α_C without further suppressing the β formation temperature [12]. In the schematic microstructures (Figure 2c,d), grey denotes α-Al dendrites, black denotes eutectic Si, red denotes platelet β-$Al_{4.5}FeSi$, turquoise outlines denote Chinese-script α_C-$Al_{15}(Fe,Mn)_3Si_2$, and solid turquoise denotes polyhedral α_C. On this basis, the present review treats phase identity, the hazardous size tail, morphology, spatial connectivity, interface integrity and the indirect effect of Fe on precipitation strengthening and matrix flow stress as distinct acceptance variables. Formation maps, scrap-compatible alloy concepts and recent reviews support this direction [1,8,9,39,40]. We identify three remaining gaps: three-dimensional damage criteria lag behind two-dimensional statis-

tics; coupled matrix-strength-particle-state datasets remain scarce; and multi-impurity Fe-Si-Cu-Zn-Mn studies are much less common than single-Fe or Fe-Mn investigations.

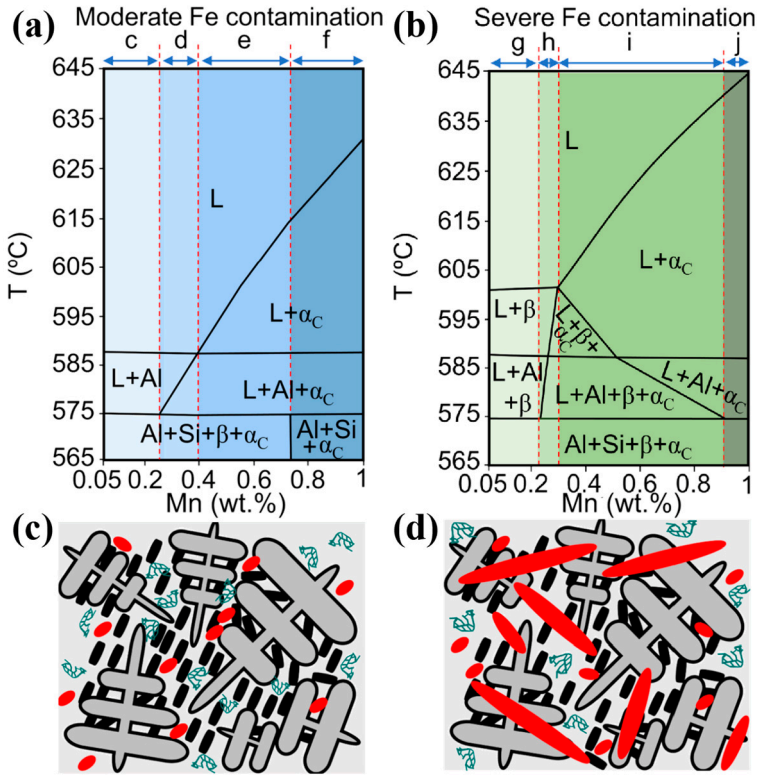


Figure 2. Composition-dependent selection of Fe-rich intermetallics. (**a**) Equilibrium isopleth for Al-11Si-0.7Fe-xMn (wt.%) with zones c–f. (**b**) Equilibrium isopleth for Al-11Si-1.4Fe-xMn (wt.%) with zones g–j. Zone c confines Fe-rich phases to the final eutectic; d partially replaces β platelets with pre-eutectic Chinese-script α_C; e–f suppress fine β but promote coarse polyhedral α_C; g forms coarse pre-eutectic or primary β; h reduces coarse β through Chinese-script α_C formation; i further refines and suppresses β while promoting polyhedral and Chinese-script α_C; and j stabilises coarse primary polyhedral. α_C without further lowering the β formation temperature. (**c**,**d**) Schematic microstructures. Grey, α-Al dendrites; black, eutectic Si; red, platelet β-$Al_{4.5}FeSi$; turquoise outlines, Chinese-script α_C-$Al_{15}(Fe,Mn)_3Si_2$; solid turquoise, polyhedral α_C. Adapted and recomposed from Ref. [12].

This review uses Fe and its coupling with Si, Mn, Cu, Cr and Zn as the organising thread and evaluates the literature through a composition-phase selection-three-dimensional microstructure-mechanical response chain. The primary scope is cast and 6xxx recycled alloys, supplemented by foundational and recent studies of phase selection, in situ and three-dimensional evolution, local damage and engineering control. Strengthening and toughening are defined operationally as the joint retention of strength, plasticity and damage tolerance; preservation of ultimate tensile strength alone is not treated as improved toughness. The review first defines impurity tolerance, then examines Fe-rich phase formation and three-dimensional structure, strengthening-damage competition, alloying and processing routes, multi-impurity coupling and computation-assisted design. It does not seek a grade-independent permissible Fe value. Instead, it explains why equal Fe contents can produce different mechanical responses through phase constitution, particle scale, spatial topology, matrix state and interface condition, and derives microstructure-based design principles that can be tested for specific alloys and processes.

2. Evolution of the Impurity-Tolerance Concept and Theoretical Framework

Traditional aluminium-alloy design begins with a target grade: the principal alloying elements and impurity ranges are prescribed, after which feedstock selection, melt treatment and processing windows are used to obtain the desired microstructure and properties. This approach assumes that feedstock composition can be controlled consistently. Post-consumer scrap converts that assumption into a probabilistic problem because Fe, Cu, Si and Zn vary among batches and may enter as correlated mixtures [1–6,8–11]. Steel fasteners and mixed aluminium grades can raise Fe in automotive scrap, whereas contamination by 2xxx/7xxx material can raise both Cu and Zn. Screening only by single-element maxima consequently forces potentially useful scrap into downcycling or primary-aluminium dilution [1,3,5,7–10,13].

We therefore define impurity tolerance as the ability of a material to retain an acceptable microstructure and service performance under impurity fluctuations for a specified alloy system, processing route and property set. This definition has three constraints. First, tolerance is property specific: yield strength, total elongation, fracture toughness and fatigue resistance may correspond to different Fe windows. Second, it is process specific: as-cast, extruded, rolled and solid-state-recycled materials can develop different particle geometries and interface states at the same Fe content [16,21,23,41–49]. Third, it depends on the matrix. In 6xxx alloys, sequestration of Si by Fe-bearing phases modifies β″ precipitation [16,33,34,50]; in Al-Si cast alloys, Fe-rich phases interact with eutectic Si, porosity and interdendritic feeding [15,21,45,51–54]; and in Cu-bearing alloys, coarse Fe-Cu-bearing constituents partition Cu away from the matrix [43,55].

To convert these constraints into a testable framework, we use a four-level chain: composition to phase selection to three-dimensional microstructure to mechanical response. Composition includes the total Fe level and ratios such as Fe/Si, Mn/Fe and Cu/Fe. Phase selection describes competition among β-Al-Fe-Si, α-Al(Fe,Mn)Si, Al_6(Fe,Mn), $Al_{13}Fe_4$ and Al_7Cu_2Fe. The three-dimensional microstructure comprises size distributions, shape anisotropy, connected networks, interparticle spacing and phase fraction. Mechanical response distinguishes matrix strengthening, load sharing, local strain partitioning, particle fracture, interface decohesion, and void growth and coalescence. Figure 3 makes this transfer explicit: the two contamination states differ in particle population and morphology (Figure 3a,b), while the corresponding orientation maps illustrate differences in grain structure (Figure 3c,d). Fe content cannot therefore be mapped directly onto performance; its effect must be traced through phase selection, spatial organisation and local deformation.

Within this chain, no single microstructural metric determines whether an impurity becomes damage critical. The upper tail of the size distribution controls the probability of extreme particles; aspect ratio and local curvature govern tip stress concentration; three-dimensional connectivity determines whether brittle phases create long-range load-transfer and damage-propagation paths; phase fraction and interparticle spacing set the density of potential initiation sites; matrix flow stress and strain-hardening capacity control load transfer and plastic accommodation; and particle-matrix interface integrity biases failure towards particle fracture or interface decohesion. Because these variables are coupled, neither a smaller mean particle size nor a more compact average morphology is synonymous with greater impurity tolerance.

This multivariable framework does not require an immediate universal model for engineering practice. Synthesising studies [1,8,9,39,40], we propose a practical hierarchy that retains Fe content as a first-level feedstock screen and risk indicator, then uses phase identity, size distribution, morphology, three-dimensional connectivity, phase fraction, matrix state and interface damage to explain performance scatter. Composition limits may

be sufficient when Fe is low and processing is stable. Microstructure-level criteria become indispensable as Fe and feedstock variability rise or as products demand high ductility, fatigue resistance and fracture safety. In this review, scrap-compatible design therefore means using phase selection and microstructural control so that variable feedstocks reproducibly attain acceptable structures and properties, rather than returning every batch to a traditional narrow composition window.

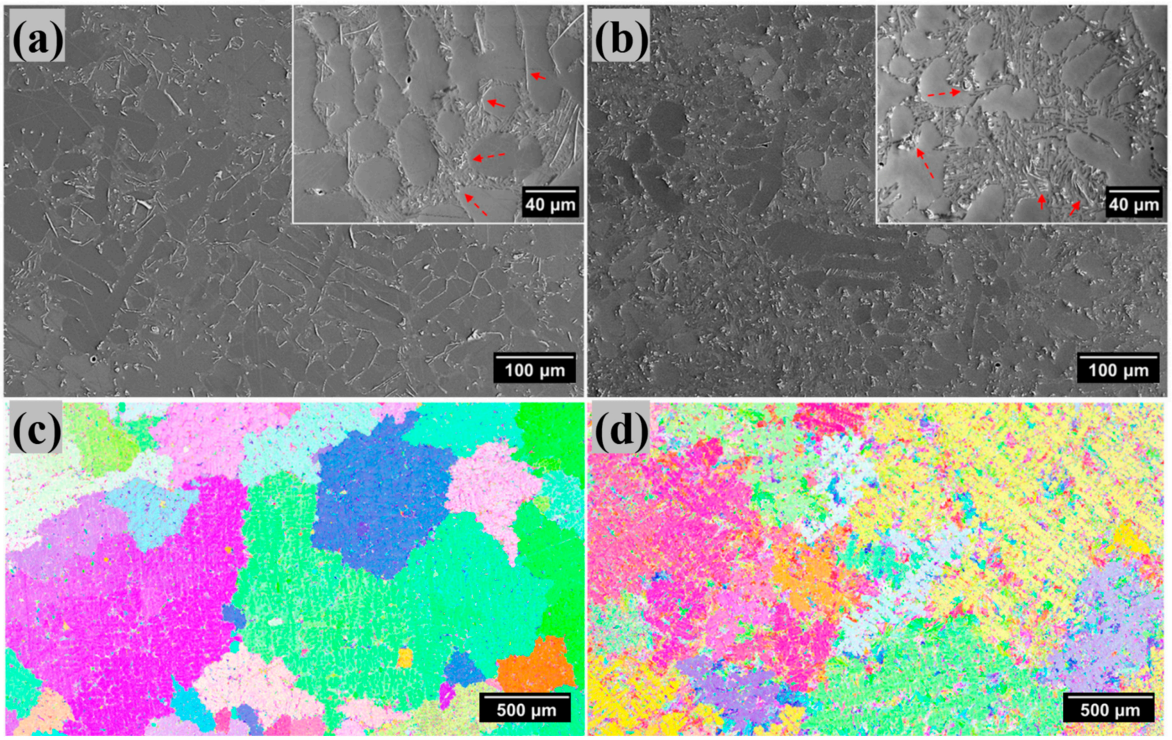


Figure 3. Morphology and grain structure in Fe-containing recycled alloys. (**a**,**b**) Backscattered-electron microstructures at two contamination levels. (**c**,**d**) Corresponding orientation maps. Adapted and recomposed from Ref. [12].

3. Formation, Evolution and Three-Dimensional Structure of Fe-Rich Intermetallics

Fe-rich intermetallics are not a single compound. Their identity is jointly determined by the concentrations of Si, Mn, Cr, Cu and Mg and by the solidification path. Plate-like β-Al-Fe-Si and α-Al(Fe,Mn)Si-type phases are common in Al-Si and 6xxx-related systems [14,15,17,50,56–60]; $Al_6(Fe,Mn)$ and $Al_{13}Fe_4$ may occur through different non-equilibrium phase-selection pathways [56,61], while historical work identified Al_6Fe [44]; and Cu-bearing cast and high-strength alloys may also contain Al_7Cu_2Fe and multicomponent compounds [43,55,61–65]. In this review, β-Al-Fe-Si and α-Al(Fe,Mn)Si denote phase families. Specific stoichiometric labels, including β-Al_5FeSi and α-$Al_{15}(Fe,Mn)_3Si_2$, are retained only when the cited study reports a corresponding phase assignment. This nomenclature is our editorial convention for avoiding compositionally invariant interpretations of nominal formulae while accommodating Mn, Cr and Cu substitution and non-stoichiometry. Liu et al. identified a Chinese-script Al_mFe phase in Al-4.6Cu-0.5Fe [63]. Historical DC-casting and controlled-solidification studies likewise examined process-dependent Al-Fe(-Si) intermetallic formation [66,67].

Phase identity is only the starting point of microstructural risk. Three-dimensional studies show that the feature often called needle-like β-Al-Fe-Si in two-dimensional metallography is generally a thin plate or lamella [14,15,45,68,69]. Chinese-script α-Al(Fe,Mn)Si

may appear as curved branches or short rods in section but can form a connected skeleton in three dimensions [49,68–70]. Faceted intermetallics also exhibit compact or polyhedral morphologies [59]. Primary α phases have cooling-dependent growth morphologies [71]. A nominally identical phase can therefore exhibit different scales and spatial topologies under different nucleation and cooling conditions. On the basis of this evidence, we treat the rule that β-Al-Fe-Si is harmful whereas α-Al(Fe,Mn)Si is beneficial as a low-order heuristic, not as a quantitative damage criterion.

Phase selection results from competition between thermodynamic stability and nucleation-growth kinetics. Mn alters the formation free energy of selected α-Al(Fe,Mn)Si phases and redistributes Fe among phases [22,56,72–75]. Si participates in Fe-Si intermetallic formation and changes the solidification path of the residual liquid, while cooling rate governs undercooling, diffusion time and nucleation density [15,17,50,60,65,74,75]. In model recycled Al-Si alloys, Becker et al. showed that Mn and cooling rate do not act additively and that rapid cooling does not guarantee elimination of plate-like phases [72]. Que et al. further found that metastable θ-$Al_{13}Fe_4$ and Al_6(Fe,Mn) can precede equilibrium α-Al_{15}(Fe,Mn)$_3Si_2$ and leave distinct geometric inheritance after transformation [56]. Tolerance design must therefore control the phase-formation pathway, not only the stable phases predicted at the terminal state.

In situ X-ray methods have converted this pathway from a post-mortem inference into a direct observation. Synchrotron imaging resolves the nucleation time, growth direction, branching and mutual contact of primary Fe-rich crystals, while four-dimensional tomography records the evolution of three-dimensional morphology. Figure 4a–d shows a population progressing from a few local units to a larger, denser and more strongly connected structure. The hazardous final topology therefore arises through continuous nucleation, growth and impingement rather than at a single instant. Feng et al. examined competition between faceted and non-faceted morphologies in high-Fe recycled aluminium, and Li et al. combined cooling rate, X-ray computed tomography (XCT) and machine learning to predict intermetallic scale [57,76]. These studies turn the empirical relation between faster cooling and refinement into a quantifiable solidification-kinetics problem.

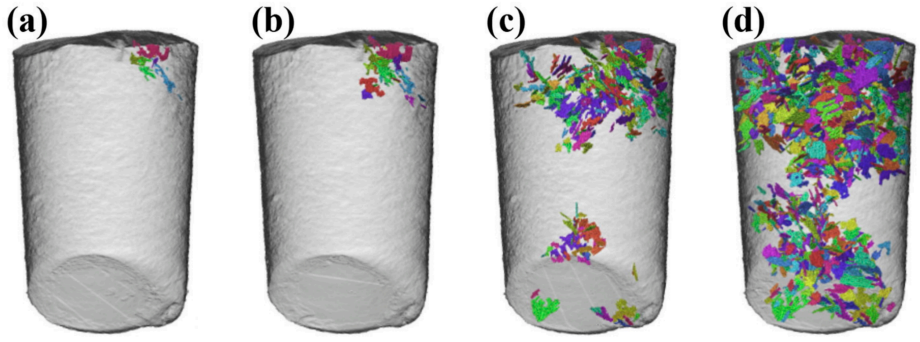


Figure 4. Three-dimensional intermetallic populations during solidification. (**a**–**d**) Reconstructed volumes showing the progressive increase in number density, size and connectivity. Adapted and recomposed from Ref. [68].

3.1. From Two-Dimensional Morphology to Three-Dimensional Structure

Two-dimensional metallography remains the lowest-cost, highest-throughput industrial method, but it introduces three systematic geometric biases for Fe-rich phases. First, a single three-dimensional plate can appear needle-like, rod-like or particle-like depending on the sectioning angle [15,45,68,69]. Second, one connected skeleton can be segmented into several apparently isolated particles in a single plane [49,59,68,69]. Third, a finite field

of view can miss the small number of extreme particles that governs the hazardous size tail [45,49,51,68,69]. Mean particle size may therefore conceal the dominant risk.

Three-dimensional XCT, focused-ion-beam scanning-electron-microscopy tomography and serial sectioning directly provide equivalent diameter, principal-axis length, volume, surface area, curvature, connected volume and skeleton branch count. Recent SRXCT studies of AA3104 and recyclable A356 independently show that Fe level changes phase thickness, branching, connectivity and damage-sensitive topology [45,49,59,77,78]. Figure 5 further shows that the three-dimensional structure records formation history. Each sequence begins with nucleation, proceeds through directional growth and branching, and ends in impingement, obstruction and coalescence (Figure 5a–d). Short rods that appear isolated in two dimensions may consequently belong to a connected body hundreds of micrometres across, with an effective loaded scale far greater than that of any single section. We therefore distinguish the hazardous size tail, which describes the extreme unit, from connectivity, which describes the larger load-bearing and damage pathway.

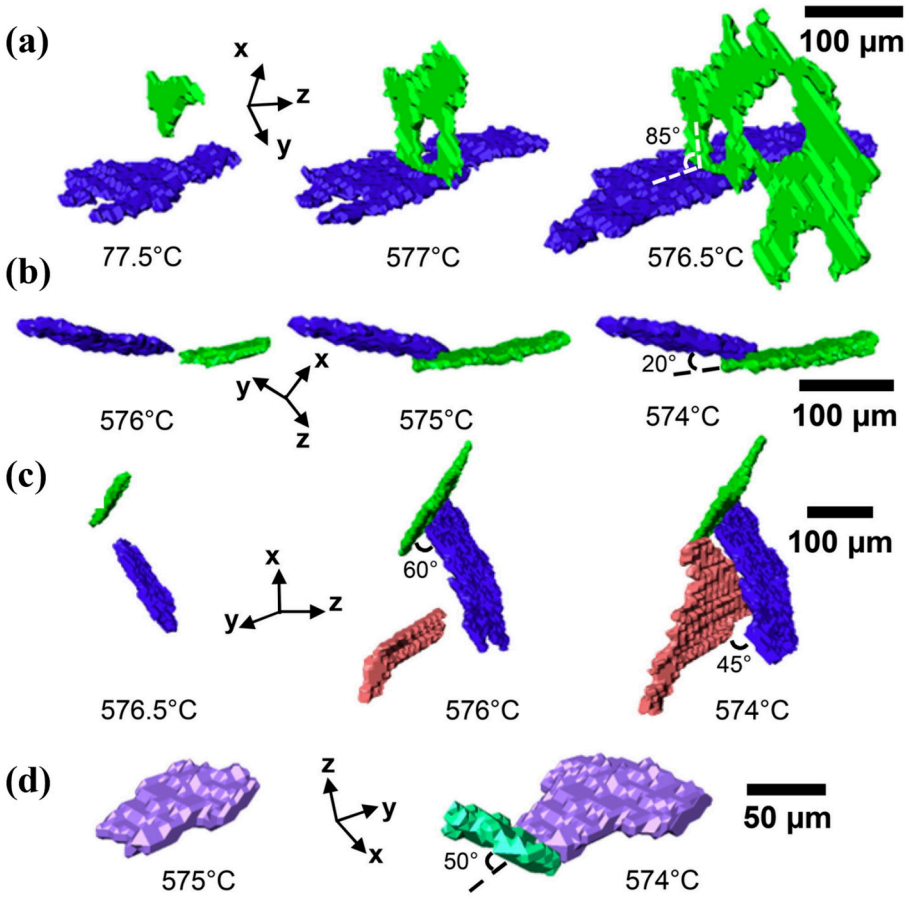


Figure 5. Temperature-resolved three-dimensional growth of Fe-rich intermetallics. (**a**–**d**) Complete reconstruction sequences showing nucleation, branching, impingement and coalescence. Adapted and recomposed from Ref. [68].

Connectivity becomes actionable only when amount, topology and span are reported separately. We recommend a minimum descriptor set. The largest-connected-component (LCC) fraction, defined as the volume of the largest connected object divided by the total Fe-rich intermetallic volume, measures how much of the phase population belongs to the dominant object. A Euler-characteristic-based connectivity density, normalised by the analysed volume, distinguishes a population of isolated particles from a multiply linked skeleton. Skeleton-length density and branch-point density describe pathway density,

whereas maximum geodesic span and directional percolation indicate whether a connected object approaches the dimensions of the sampled volume or the principal loading path. No single descriptor is sufficient: a compact cluster can have a high LCC fraction but limited span, whereas a sparse branched object can occupy less volume yet extend across a mechanically relevant distance. Fractal dimension may supplement this set but is more sensitive to scale range and segmentation. All metrics must therefore be accompanied by voxel size, region-of-interest dimensions, segmentation threshold and minimum retained object volume [68,69].

Three-dimensional characterisation also changes how phase fraction should be interpreted. A two-dimensional area fraction approximates volume fraction only for random sections with adequate sampling. Error increases when Fe-rich phases are strongly oriented, plate-like or networked [45,49,59,68,69]. After thermomechanical processing elongates, rotates or fragments particles along the rolling or extrusion direction, two-dimensional results also depend strongly on the sampled plane. Comparative tolerance studies should therefore report both processing and transverse sections and calibrate two-dimensional bias by XCT for critical samples. We recommend that, where three-dimensional data are unavailable, connectivity be identified explicitly as unmeasured rather than inferred from two-dimensional spacing.

3.2. Mechanical Consequences of Three-Dimensional Connectivity

The first mechanical consequence of connectivity is an enlarged effective geometric scale. An isolated particle can be described by its principal axis or equivalent diameter, whereas a network must be characterised by its dominant connected fraction, topology and effective span rather than by mean size alone. Fe content, cooling rate, Mn/Cr level and nucleation conditions can change this effective scale substantially even when mean particle size changes little [45,49,51,59,67–70]. Geometric characterisation must therefore establish the effective network scale, and mechanical characterisation must determine when that scale produces particle cracking, voids and macroscopic fracture under a specified load.

Connectivity also couples different second phases and defects spatially. Fe-rich phases can co-segregate with eutectic Si, Al_2Cu-type phases, oxide films, shrinkage cavities and gas pores in interdendritic regions. Coarse plates can restrict feeding, while oxide films may serve as heterogeneous nucleation substrates. An increase in Fe-rich phases and an increase in porosity are therefore not always independent events [51–54,79,80]. Treating porosity and Fe-rich area fraction as unrelated scalars misses the mechanically more relevant question of whether they contact one another and form a serial weak zone [38,51–53,79,80].

Three-dimensional connectivity is thus a geometric amplifier rather than a stand-alone fracture criterion. A network enlarges the distance over which elastic–plastic mismatch can propagate and makes a crack in one particle more likely to interact with neighbouring particles, pores or oxide films. Further propagation nevertheless remains constrained by matrix load-bearing capacity, strain hardening and particle-matrix interface integrity. A complete assessment must connect network formation and effective scale to cracking, void growth and crack linkage under the relevant loading path.

3.3. Competition Among Multiple Phase-Selection Pathways

The three-dimensional differences described above originate in competition among the phase-selection pathways themselves. This section therefore separates what the structures are (Sections 3.1 and 3.2) from why they form, and considers both thermodynamic and kinetic drivers. The common shorthand that Mn converts β-Al-Fe-Si to α-Al(Fe,Mn)Si omits at least three stages: nucleation, growth and subsequent transformation. Figure 6 places these stages on a common temperature axis. The sharp increase in intermetallic

number on or near α-Al dendrites at a lower temperature shows that the nucleation substrate changes during solidification (Figure 6a). Measured intermetallic fractions depart from a simple Scheil trajectory and depend on holding time, revealing a kinetic window for precipitation before the Al-Si reaction (Figure 6b). Chemical driving forces rank the thermodynamic tendency of candidate phases, whereas the phase-dependent interface contribution modifies the actual nucleation barrier (Figure 6c,d). In the study summarised in Figures 6 and 7, Mohammed et al. performed CALPHAD and Scheil-Gulliver calculations with Thermo-Calc 2022b using the TCAL5.1 aluminium-alloy database [12,81,82]. Related studies of θ-$Al_{13}Fe_4$, Al_6(Fe,Mn) and α-Al_{15}(Fe,Mn)$_3Si_2$ show that metastable precursors can form first and that the Al6-to-α transformation retains geometric inheritance [12,56,68]. An α-Al(Fe,Mn)Si-dominated final state therefore does not imply that high-aspect-ratio precursors were absent during solidification.

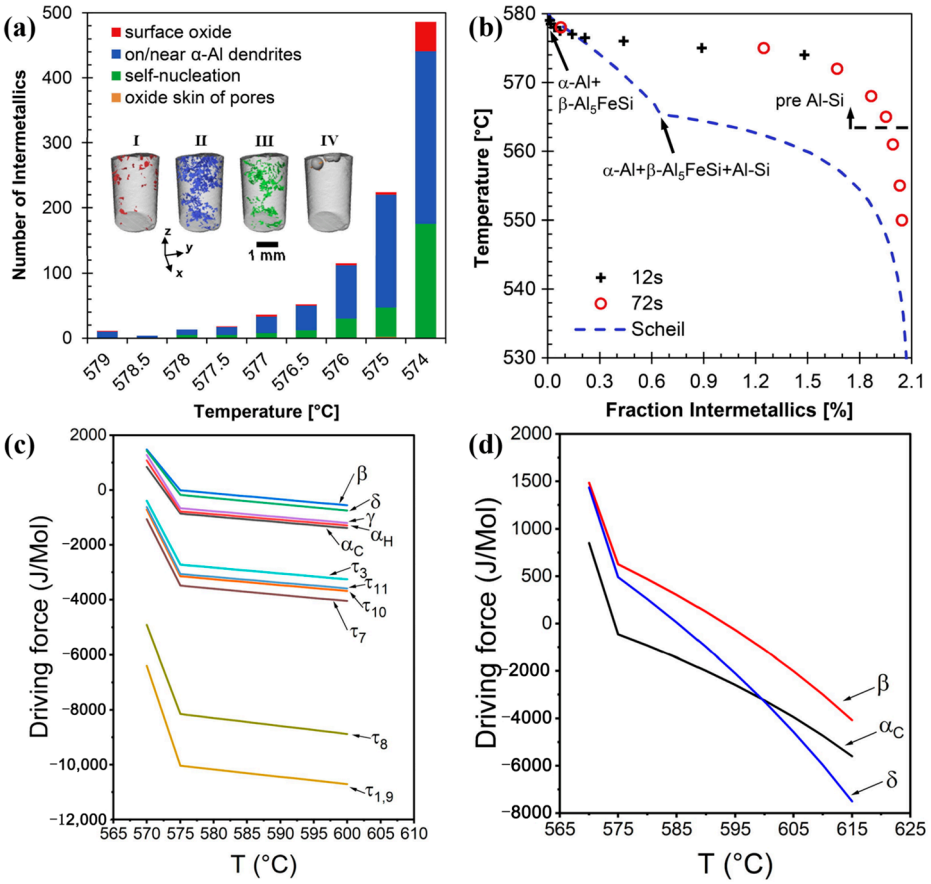


Figure 6. Thermodynamic and kinetic descriptors of intermetallic formation. (**a**) Temperature-dependent distribution of nucleation sites. (**b**) Measured intermetallic fraction at two holding times compared with the Scheil path. (**c**) Chemical driving forces of candidate Fe-rich phases. (**d**) Phase-dependent driving-force contribution associated with interfacial energy. Adapted and recomposed from Refs. [12,68].

Composition and interface conditions jointly determine which pathway prevails. The Fe-Mn-Si response maps in Figure 7a,b show how Si and Mn change the critical Fe content and the corrected fraction. Figure 7c gives the calculated solid–liquid interfacial energies for the ternary-eutectic moderately contaminated alloy Al-12.67Si-0.89Fe (wt.%), whereas Figure 7d gives the corresponding values for the far-from-eutectic severely contaminated alloy Al-7Si-2Fe (wt.%) [12]. The same Mn addition may therefore be beneficial, redundant or detrimental depending on the Fe and Si background. In both composition states, the interfacial energies of α_H, α_C, γ, δ and β phases are sufficiently close for the

ordering of competing nucleation barriers to matter. Similar chemical driving forces do not therefore guarantee the same nucleation sequence. Together, the four panels show that phase selection is governed by competition among composition-dependent driving force, interface-controlled nucleation barrier and the cooling-controlled time window, rather than by the Mn/Fe ratio alone [12].

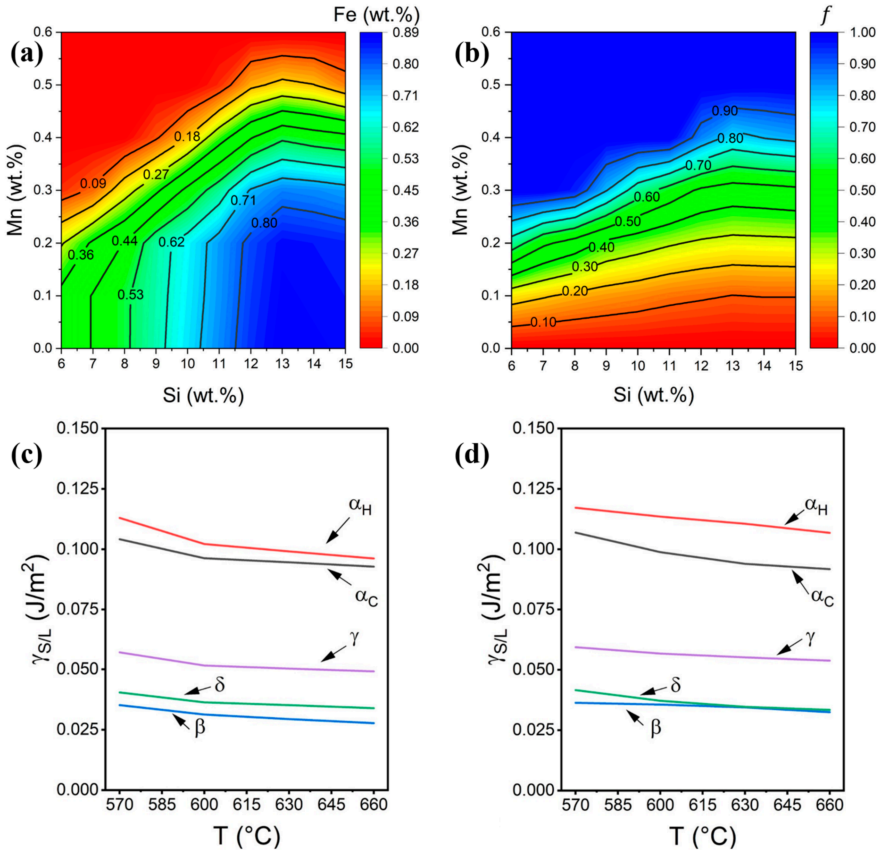


Figure 7. Competing phase-selection pathways. (**a**) Critical Fe-content map and (**b**) corrected-fraction map across the Fe-Mn-Si design space. (**c**) Temperature-dependent solid–liquid interfacial energies for Al-12.67Si-0.89Fe (wt.%), a ternary-eutectic moderately contaminated composition. (**d**) Corresponding interfacial energies for Al-7Si-2Fe (wt.%), a far-from-eutectic severely contaminated composition. Adapted and recomposed from Ref. [12].

Kinetic boundaries are also affected by nucleation substrates and cooling conditions. TiB2, TiC, oxide films and pre-existing intermetallics can lower the nucleation barrier for selected Fe-rich phases. B, Ti and grain refiners may increase nucleation density and reduce individual particle size, but can also raise phase fraction or change the spatial relation between particles and α-Al grains [83–85]. Rapid solidification has a similar dual effect. Short diffusion distances and higher nucleation rates usually refine Fe-rich phases and extend Fe supersaturation in α-Al, but may stabilise metastable phases that are disfavoured during slow cooling. Additive manufacturing, strip casting and rapidly quenched model alloys are therefore useful for exploring high-undercooling limits, although their phase constitution cannot be transferred directly to conventionally cast recycled aluminium [22,75,86–88]. Warmuzek et al. examined Mn-dependent peritectic transformation in Al-rich Al-Fe-Mn-Si alloys [89]. Kumar and O'Reilly investigated the influence of Al grain structure on Fe-bearing intermetallic formation during DC casting [90].

4. Competition Between Strengthening and Damage

The mechanical role of Fe-rich phases depends strongly on microstructural state. Figure 8a shows that strength and fracture elongation do not change in fixed proportion when composition or microstructure changes. The accompanying panels show cracks through platelet and Chinese-script Fe-rich phases near the fracture surface (Figure 8b–d) [12]. This juxtaposition of macroscopic load bearing and local damage explains the apparent contradiction: fine, dispersed particles can alter grains, dislocation structures and load partitioning, whereas coarse, sharp or connected particles are high-probability initiation sites for voids and cracks [12,34–38,45–49,80,91–93]. Strength tolerance and damage tolerance can therefore evolve in different directions. Yield and ultimate tensile strengths may remain acceptable even after total elongation, bendability or fracture behaviour has deteriorated [12,34–36,38,46–48,91–93].

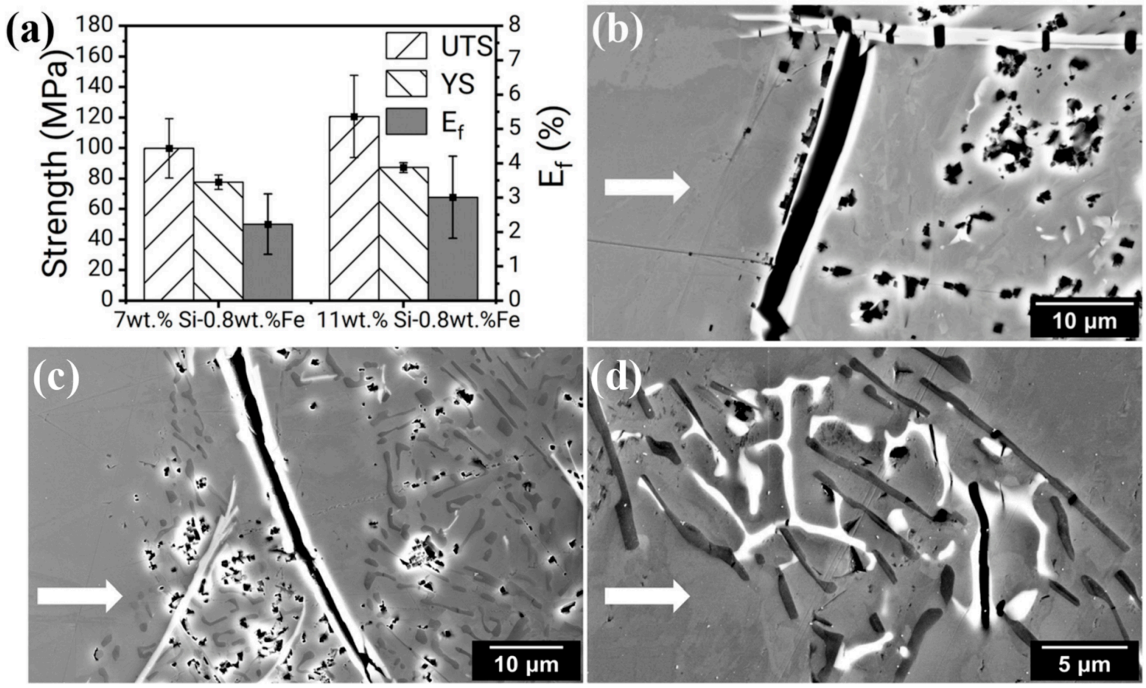


Figure 8. Tensile properties and cracking through Fe-rich intermetallics. (**a**) Ultimate tensile strength, yield strength and fracture elongation of Al-7Si-0.8Fe and Al-11Si-0.8Fe (wt.%). (**b**,**c**) Cracking through platelet Fe-rich phases in the Al-7Si alloy. (**d**) Cracking through Chinese-script Fe-rich phases in the Al-11Si alloy. White arrows indicate the tensile direction. Adapted and recomposed from Ref. [12].

4.1. Microstructural Origins of Strengthening

Micrometre-scale Fe-rich particles cannot be treated as nanoscale Orowan obstacles. Duchaussoy et al. investigated ultrafine-grained Al-Fe stabilised by nanoscaled intermetallic particles [41]; this regime should be distinguished from coarse constituent particles. Around micrometre-scale particles, elastic–plastic mismatch generates local strain gradients [35,37,38]. Their contribution to strength must therefore be evaluated together with local damage.

In 6xxx alloys, the competition also involves redistribution of the solute reservoir. Fe-rich phases and subsequently formed α-Al(Fe,Mn)Si dispersoids consume Si and thereby modify β″ precipitation [16,32–34,50]. The net strength effect of Fe includes grain refinement and particle-stimulated nucleation, heterogeneous deformation, changes in dispersoid content and loss of strengthening precipitates, while ductility additionally depends on hazardous particle geometry and connectivity. Recycled AA6016 containing approximately

0.40 wt.% Fe retained a response close to the low-Fe reference; at higher Fe, primary intermetallic networking and a reduction in β″ precipitates occurred concurrently [34]. The resulting strength change cannot be assigned to either particle strengthening or precipitation loss alone.

We treat the matrix state as a boundary condition for assessing the strengthening-damage balance. Load transfer and plastic accommodation around particles depend on matrix flow stress, strain hardening and the local stress state [37,38,46–48,91]. These variables must be considered together with particle strength and interface integrity; the cited studies do not establish a universal critical matrix strength.

4.2. Damage Initiation and Evolution Pathways

Fe-rich particles initiate damage through two principal routes: fracture within the particle and decohesion at the particle-matrix interface. The dominant route depends on particle strength, size, morphology and crystallographic orientation, interface bonding, matrix flow stress and local stress triaxiality. Coarse plates and sharp tips generally produce stronger stress concentrations, but size alone is not sufficient [37,38,46–48,91–94]. In situ tension and HRDIC show highly scattered cracking strains even within a narrow size range because local orientation, particle clustering and neighbouring slip bands alter the failure sequence [35,37,38,91,94].

Figure 9 illustrates deformation heterogeneity around Fe-rich particles. From left to right, the panels show the particle neighbourhood, geometrically necessary dislocation density, orientation deviation and lattice rotation about the z axis. These EBSD maps reveal an inhomogeneous matrix response, rather than being direct strain maps [35]. This evidence complements the HRDIC and tomography results from recycled IBA6111, which retains an ultimate tensile strength of about 328 MPa and uniform elongation of about 21%, yet shows particle-neighbourhood damage and faster post-necking void growth and coalescence [35,36].

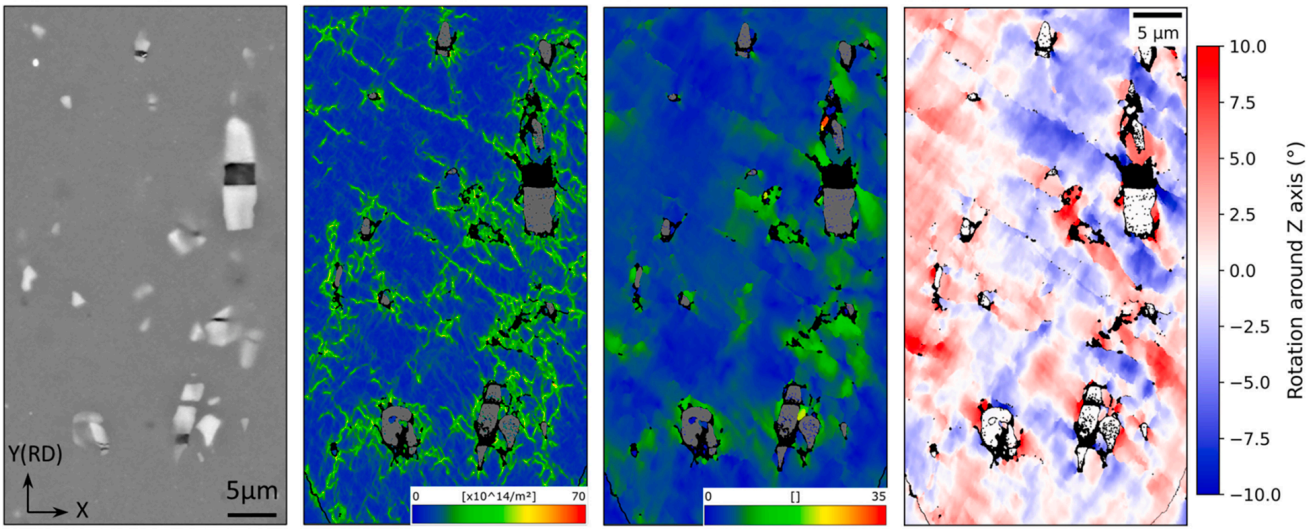


Figure 9. Local deformation heterogeneity around Fe-rich particles. From left to right: particle neighbourhood, geometrically necessary dislocation-density map, orientation-deviation map, and lattice rotation about the z axis. Adapted and recomposed from Ref. [35].

Interface integrity influences whether damage begins inside a particle or at the particle-matrix boundary [91]. Figure 10a shows effective-strain and rotation fields at successive strain levels; Figure 10b combines the initial microstructure and grain map with observations at necking and fracture; and Figure 10c shows a cracking particle and its associated void. Particle-diameter and sphericity distributions compare cracked and uncracked pop-

ulations in Figure 10d [35,36]. Geometry changes cracking susceptibility but does not determine the fate of every individual particle [35,37,38]. Oxide films and inherited chip boundaries introduce an additional interface constraint in recycled material: particle refinement must be accompanied by effective consolidation of chip boundaries [95–101].

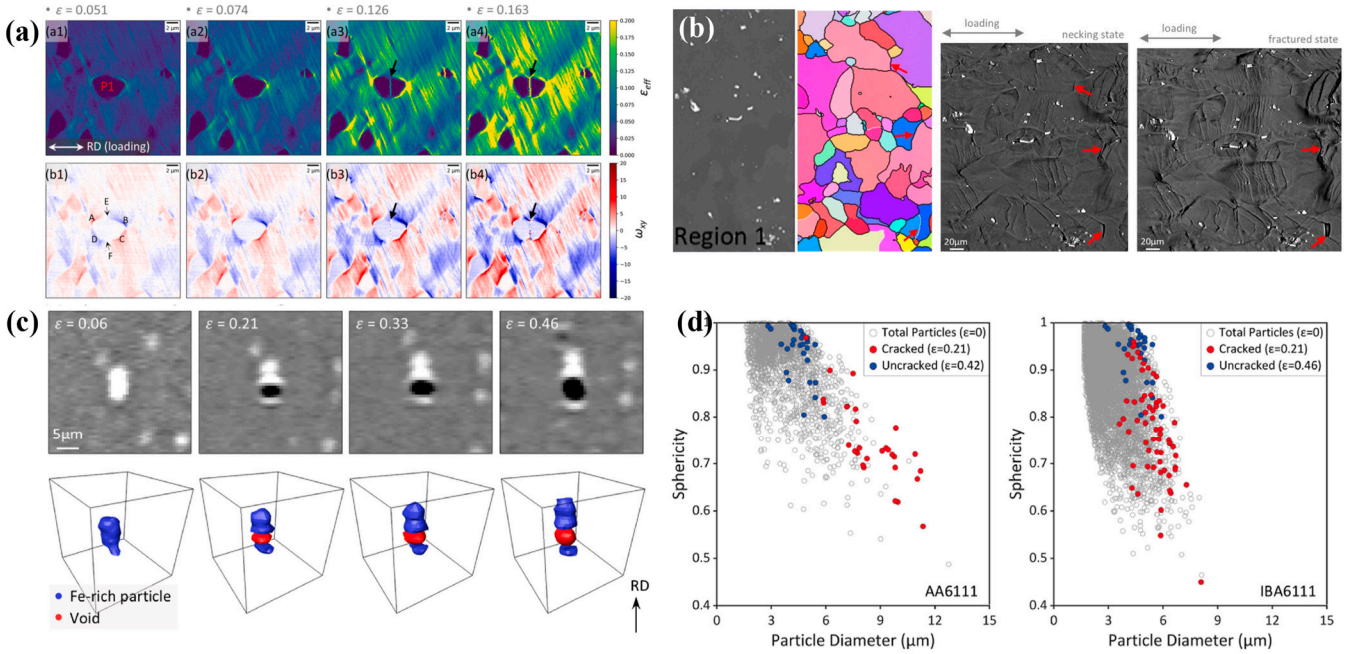


Figure 10. Particle cracking and void nucleation during deformation. (**a**) Effective-strain and rotation fields at successive strain levels. (**b**) Initial microstructure and grain map, with SEM observations at necking and fracture. (**c**) Two-dimensional views and three-dimensional reconstructions of a cracking particle and its associated void; blue denotes the Fe-rich particle and red the void. (**d**) Particle-diameter and sphericity distributions comparing cracked and uncracked populations in AA6111 and IBA6111. Adapted and recomposed from Refs. [35,36].

A two-dimensional section cannot determine whether early voids form a dominant three-dimensional fracture path. The upper panels of Figure 11 compare particle populations in commercial AA6111 and recycled IBA6111. The lower-left panel reconstructs intermetallic particles in blue and voids in red, while the lower-right panels follow void evolution with strain [36]. A higher density of damage sites reduces void spacing and promotes interaction during necking; acceptable uniform elongation therefore does not imply equivalent total elongation or residual damage reserve [36–38]. Fatigue cracks and toughness losses may also be controlled by extreme particles, pores or spatial combinations of both [38,46–48,80,93,102–106]. Conversely, Blind and Martin found that a higher dispersoid volume fraction could increase the ductile fracture toughness of peak-aged Al-Mg-Si alloys at similar grain size and yield strength by homogenising slip, illustrating the additional role of matrix deformation [107].

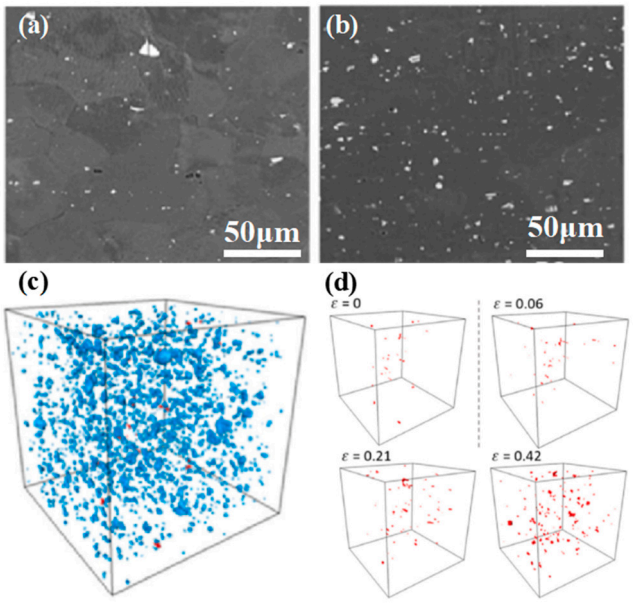


Figure 11. Fe-rich intermetallic populations and void evolution. (**a**,**b**) representative microstructures of commercial AA6111 and recycled IBA6111. (**c**) three-dimensional reconstruction of intermetallic particles (blue) and voids (red). (**d**) strain-resolved reconstructions of void evolution [36].

4.3. Conditions Governing the Strengthening-to-Damage Transition

Building on the experimental evidence above, this section synthesises the strengthening-to-damage transition into three operational microstructural dimensions, namely the hazardous size tail, shape anisotropy and three-dimensional connectivity, while treating the matrix strength and interface state as boundary conditions. Current evidence does not support an alloy-independent critical particle size or aspect ratio [35,37,38,46,47,91]. High-percentile size metrics are more relevant than the mean to extreme-value-controlled fracture, but particles with the same size tail can still differ because sharp plates and compact polyhedra have different local curvatures [35,37,38,91]. Likewise, isolated particles and three-dimensional networks can have different effective loaded scales despite similar two-dimensional aspect ratios. The transition is consequently probabilistic and shifts with phase identity, matrix strength, interface condition and stress state [35,37,38,46–48,80,91,93].

Figure 12 quantifies particle cracking through the observed cracked-particle fraction. The cracked-particle fraction rises with global strain, but at different rates in the two 6111 alloys (Figure 12a). The corresponding full-field maps show that localisation paths are jointly controlled by particle density, particle clusters and grain boundaries (Figure 12b,c), and that continuous high-strain channels can form where particle groups approach grain boundaries (Figure 12d) [35]. The benefit of size refinement must therefore be judged together with phase fraction, interparticle spacing and spatial clustering. In recycled Al-9Si-1Fe, Cr/Mn additions and cooling conditions changed plate-like or Chinese-script phases into more compact polygonal morphologies, yet elongation did not necessarily increase. A greater phase fraction, shorter spacing or other microstructural penalties can offset improved shape [45,75,93,108].

The transition from strengthening to damage is therefore not set by a single size or aspect-ratio threshold. For a defined alloy, matrix state and loading path, assessment must jointly consider the hazardous size tail, local curvature, three-dimensional connectivity, second-phase population, matrix load-bearing capacity and interface integrity. Fe-rich phases become fracture-controlling damage sources only when these factors collectively raise the probability of particle fracture or decohesion, reduce void spacing and promote void coalescence.

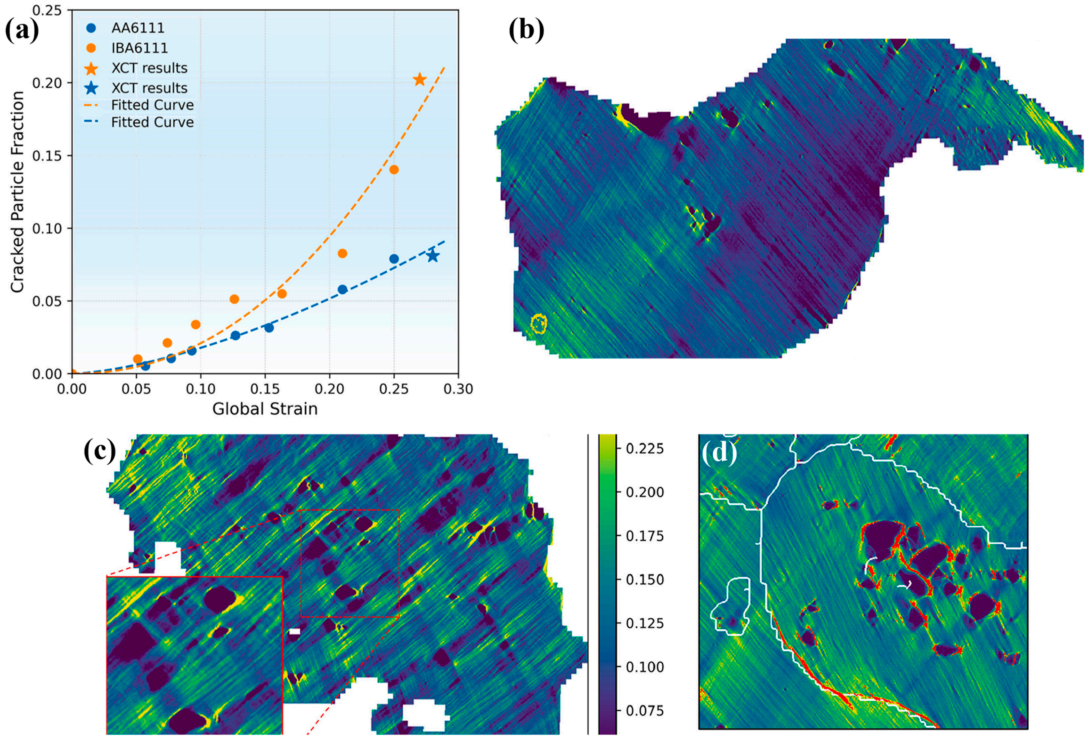


Figure 12. Observed particle cracking and strain localisation. (**a**) Cracked-particle fraction as a function of global strain in AA6111 and IBA6111. (**b**,**c**) Representative full-field strain maps. (**d**) Strain localisation around a particle cluster and nearby grain boundaries. Adapted and recomposed from Ref. [35].

5. Routes for Engineering Impurity Tolerance

Engineering strategies for Fe fall into two classes: reducing the Fe that enters the final material, or changing its microstructural state at the approximately constant total Fe. The first includes sedimentation, filtration and separation of Fe-rich intermediate phases [4,13,18–20]. Mn-assisted Fe removal has also been studied in Al-7.0Si-2.4Fe [109]. The second includes alloying, cooling control, external fields, heat treatment, deformation and solid-state recycling [16,20,27–29,72,80,95–101,108,110–115]. This review focuses on the second class because successful modification cannot be established from a change in mean particle length alone. Phase identity, the hazardous size tail, morphology, three-dimensional connectivity, phase fraction, matrix state and interface condition collectively determine whether the damage pathway has changed [37,38,45,48,49,59,72,80,93,95,108,111,112].

5.1. Alloying Strategies

Mn is the most widely used modifier of Fe-rich phases, but describing it as neutralising Fe is inaccurate. Mn does not remove Fe; it changes the thermodynamic stability, nucleation pathway and composition of Fe-rich intermetallics. It commonly shifts high-aspect-ratio plates towards Chinese-script or more compact morphologies and can reduce the hazardous size tail when a higher nucleation density restricts growth [15,17,60,72,74,75,116–119]. At the same time, the number and total fraction of α-Al(Fe,Mn)Si-type phases may increase. Mn modification therefore combines reduced plate formation, refinement of extreme particles and a larger second-phase population. Its net mechanical benefit depends on whether the first two effects outweigh increased phase fraction and solute competition [17,72,74,75,116–119].

No universal optimum Mn/Fe ratio exists independently of Si content and cooling rate. Figure 13a,b compares near-wall microstructures of Al-7Si-2Fe-0.5Mn and Al-11Si-2Fe-0.5Mn (wt.%), not a before–after pair. The former contains fine particles surround-

ing Chinese-script agglomerates, whereas the latter contains fine particles surrounding coarser polyhedral agglomerates. The phase map identifies constituents in the Al-7Si alloy (Figure 13c). The size comparison with Mn-free alloys shows that Mn did not further reduce the already refined, non-agglomerated near-wall particle sizes (Figure 13d), unlike its effect on large platelets at the cast centre discussed with Figure 14 [12]. Results from Becker et al. and Mohammed et al. thus show that additional Mn can be beneficial, redundant or a source of new coarse-phase risk under different conditions [12,72]. We therefore propose targeting the hazardous particle-size tail and connected structures within a defined Fe-Si-cooling-rate domain.

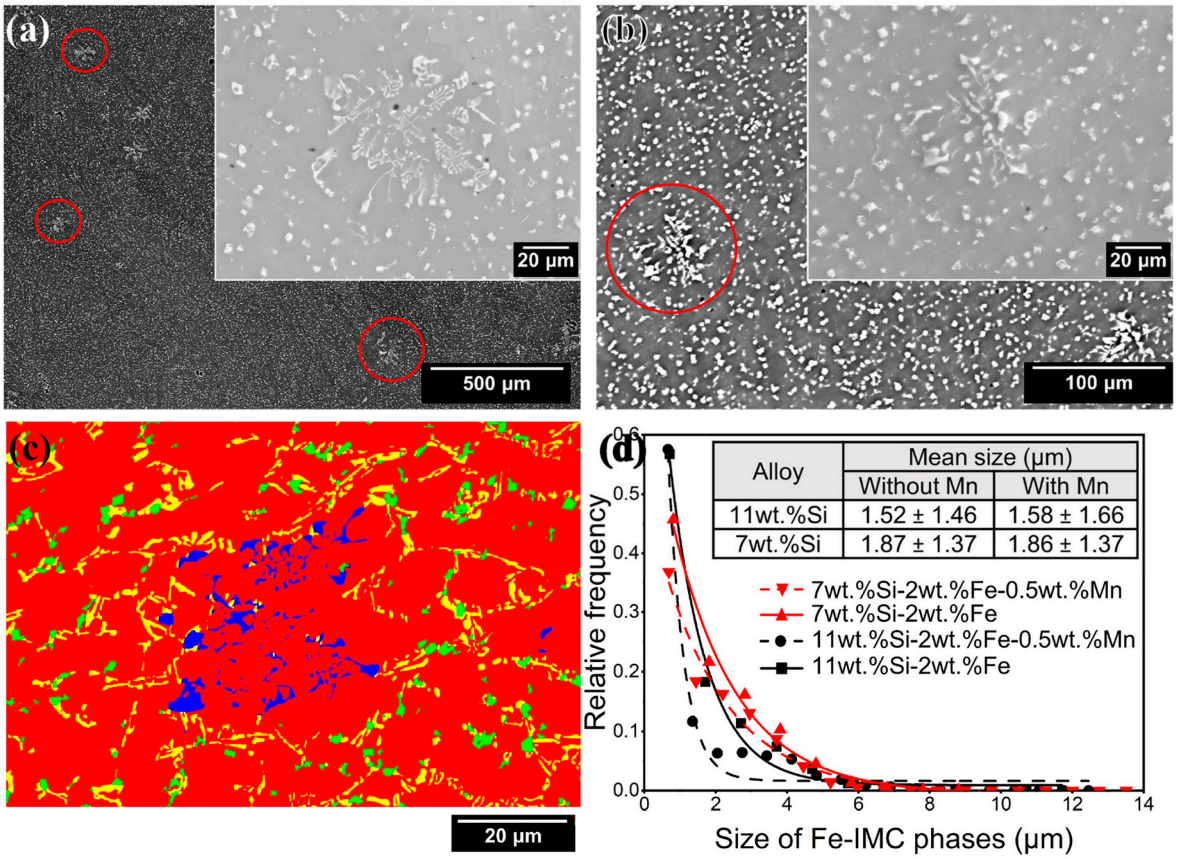


Figure 13. Near-wall microstructures of severely Fe-contaminated Al-Si alloys after adding 0.5 wt.% Mn. (**a**) Al-7Si-2Fe-0.5Mn, with fine polyhedral particles surrounding Chinese-script agglomerates. (**b**) Al-1Si-2Fe-0.5Mn, with fine particles surrounding coarser polyhedral agglomerates. (**c**) EBSD phase map of the Al-7Si alloy. (**d**) Size distributions and mean sizes of non-agglomerated Fe-rich phases near the wall, with and without Mn. All compositions are in wt.%. Adapted and recomposed from Ref. [12].

Cr can cooperate with Mn to promote selected α-Al(Fe,Mn)Si-type Fe-rich phases, but it can also increase the risk of coarse sludge particles. If a lower aspect ratio is accompanied by high-melting primary particles, both the hazardous size tail and phase fraction increase. This trade-off is evident in recycled Al-9Si-1Fe, where Cr/Mn additions and cooling conditions jointly determine plate-like, Chinese-script and polygonal morphologies, but greater compactness does not guarantee higher elongation [17,74,75,108]. Cr modification must therefore be assessed for coarse sludge formation rather than judged solely by a reduction in aspect ratio.

Sr has a well-established effect on eutectic Si, but its influence on Fe-rich phases is alloy dependent. Studies of recycled Al-9Si-0.6Fe and related alloys show that Sr can modify intermetallic nucleation and morphology, with the outcome depending on Sr level, Mn

content and cooling rate [120–124]. Sr should not, therefore, be described as converting all β-Al-Fe-Si into globular particles. The evidence supports a narrower conclusion: Sr changes Fe-rich phase size and morphology and can indirectly alter interfaces and local damage through porosity, oxide films and the eutectic-Si morphology.

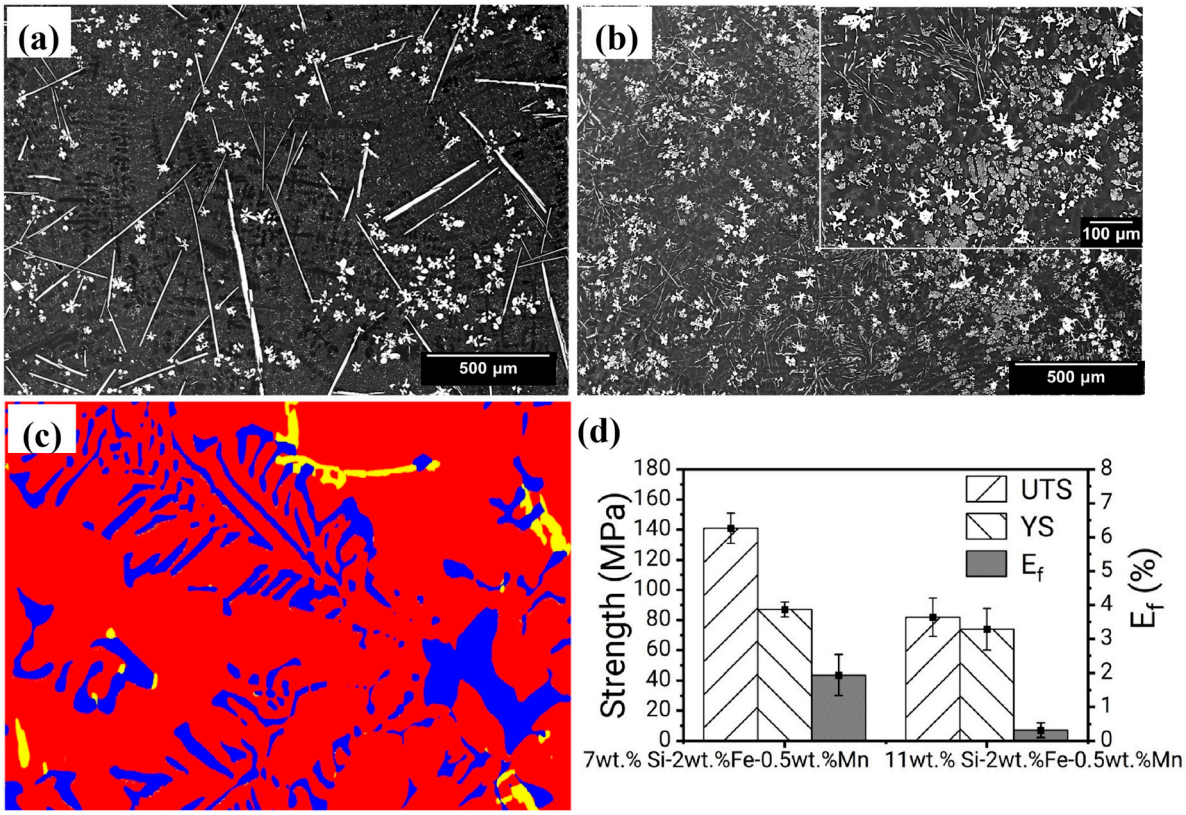


Figure 14. Composition-dependent microstructure-property response after adding 0.5 wt.% Mn to severely Fe-contaminated alloys containing 2 wt.% Fe. (**a**) Near-eutectic Al-11Si alloy retaining coarse platelet and polyhedral phases. (**b**) Far-from-eutectic Al-7Si alloy containing shorter platelets, a highly branched Chinese-script constituent and neighbouring polyhedral particles. (**c**) EBSD phase map of the branched and polyhedral Fe-rich constituents in the Al-7Si alloy. (**d**) Ultimate tensile strength, yield strength and fracture elongation of the two Mn-containing alloys. Adapted and recomposed from Ref. [12].

B/Ti-based inoculation and rare-earth modification act at different stages. B changes heterogeneous nucleation on selected substrates, and Mn + B can influence both phase stability and nucleation density [125,126]. La, Ce, Y and Nd more often affect intermetallic size and morphology through interfacial energy, local solute distribution and the solidification structure [92,127–134]. For either route, refinement becomes a robust strengthening-toughening benefit only if it compresses the hazardous size tail without creating new coarse compounds, substantially increasing phase fraction or excessively consuming strengthening solute. Sc modification has also been investigated in squeeze-cast Al-7Si-0.3Mg [110], while impurity-dependent precipitation kinetics have been examined separately in dilute Al-Sc alloys [135].

5.2. Solidification Control

Cooling rate is the most direct process variable for controlling the hazardous size tail. Increasing it generally raises undercooling, shortens diffusion and growth time, refines Fe-rich phases and may change phase selection [15,22,56,65,72–75,136]. The results of Becker, Que and co-workers nevertheless show that phase selection does not vary

monotonically with cooling rate [56,72]. Faster cooling usually compresses coarse particles and network scale, but cannot by itself guarantee a low-risk phase constitution. Studies of AA6063 and later XCT work show simultaneous changes in phase identity, particle size and three-dimensional connectivity [22]. This is why secondary dendrite arm spacing alone is insufficient: at the same spacing, different Mn/Si states can still produce different Fe-rich phases.

Ultrasonic treatment increases heterogeneous nucleation and disrupts growth boundary layers through acoustic cavitation, streaming and local perturbations of temperature and concentration. Studies in pure Al, Al-Cu and Al-Si provide complementary evidence for grain and eutectic refinement [137–141]. High-intensity ultrasound shortens coarse plates and improves spatial uniformity in high-Fe Al-Si and wrought-alloy systems [111,113–115,142]. At 2000 W, Zhang et al. reported pronounced suppression of long β-Al5FeSi plates and the appearance of fine Chinese-script phases. Ultimate tensile strength increased from 148 to 188 MPa and elongation from 1.26% to 1.90% at room temperature; at 200 °C, the corresponding changes were 141 to 165 MPa and 2.08% to 2.88% [111]. The mechanistic question is not whether total phase fraction decreases monotonically, but whether ultrasound compresses the hazardous size tail, shape anisotropy and connected network.

Electromagnetic stirring, high-shear melt conditioning and melt-conditioned direct-chill casting act through melt flow, thermal homogenisation, grain-refiner dispersion and particle collision [143]. Shiga et al. directly observed α-Al(Fe,Mn)Si evolution during electromagnetic stirring by in situ X-ray imaging [144]. High-shear methods can modify Fe-rich nucleation and scale and can also assist in the separation of Fe-rich particles [20,23,80,144–149]. When used for microstructural control, their primary outputs are particle size, morphology and spatial connectivity. When they also lower melt Fe, the route becomes a hybrid of purification and tolerance design. Experiments and performance attribution should report these contributions separately. Mechanical mould vibration also changes eutectic-Si morphology, with refinement or coarsening depending on amplitude [150].

5.3. Thermomechanical Processing and Solid-State Recycling

Fe-rich phases are not completely frozen after solidification. Homogenisation can promote selected transformations from β-Al-Fe-Si to α-Al(Fe,Mn)Si-type phases, dissolve local non-equilibrium phases and modify particle roundness. Work on solution treatment, β-Al5FeSi decomposition and interrupted homogenisation in Al-Si and 6xxx alloys demonstrates fragmentation, dissolution and transformation kinetics in the solid state [24–29,31–33,61,64,112]. These processes simultaneously change morphology, size and phase partitioning and affect matrix strengthening through Mn/Si redistribution and dispersoid precipitation [27–33,61,64]. Homogenisation should therefore be evaluated not only by the reduction in β-Al-Fe-Si area fraction, but also by particle number, the hazardous size tail and any additional loss of solute needed for subsequent ageing. Annealing-related Fe precipitation has also been studied separately in commercial-purity aluminium [30].

Extrusion, rolling and friction-stir processing can fragment coarse intermetallics and redistribute the particles. Their clearest benefit is to compress the hazardous size tail and sever pre-existing three-dimensional networks [28,49,95,151]. Fragmentation also creates fresh surfaces, however, and local interface integrity may initially decline if the matrix does not fully encapsulate these surfaces or if particles are already microcracked. Friction-stir processing of alloy 6056 shows that fragmentation and redistribution of coarse second phases can reduce fracture controlled by extreme particles [151]. The ductility benefit therefore reflects the net balance among particle refinement, network disruption and healing of newly created interfaces.

Conventional recovery of aluminium turnings may involve salt-flux melting [152], including cold compaction followed by remelting [153]; these routes should be distinguished from solid-state consolidation. Shear-assisted processing and extrusion, friction extrusion and direct chip extrusion avoid complete remelting and resolidification, preventing renewed solidification growth of coarse Fe-rich phases [95,96,98–101]. Intense shear also fragments inherited particles and consolidates chip boundaries [96,98–101]. Spark plasma sintering provides a distinct consolidation route without remelting [97]. A 2026 friction-extrusion study found that yield and ultimate tensile strengths remained close to those of material without added Fe at approximately 0.9 wt.% Fe, although ductility decreased as Fe increased [95]. The process broadens strength tolerance without eliminating damage and ductility limits. Particle pre-cracking and chip-boundary bonding remain important constraints [95,98,101].

5.4. Synergy Among Processing Routes

No single intervention is likely to optimise phase identity, size, connectivity, phase fraction, matrix and interface state simultaneously. We therefore divide the control chain into five tasks: phase selection, size control, network disruption, matrix strengthening and interface restoration. These tasks can then be assigned to different processing stages according to scrap composition and target properties. Mn/Cr primarily changes phase selection and morphology before solidification; rapid cooling and ultrasound compress coarse particles and networks; homogenisation adjusts phase partitioning and matrix state [24–29,31–33,61,64]; extrusion or rolling further fragments and redistributes second phases [28,49,95,96,98–101,151]; and ageing restores or rebuilds precipitation strengthening. In a model 6082 alloy containing 1.0 wt.% Fe, Ti solute, chemical grain refinement and high-intensity ultrasound interacted strongly, so their individual effects could not be added linearly [142].

Table 1 shows that the best process is not an extreme value of one parameter, but a path combining multistage microstructural controls. Two treatments can both increase elongation through different dominant routes: one may compress the hazardous size tail, while another improves interface integrity or redistributes matrix strengthening. From the evidence summarised in Table 1, we infer that only by separating phase selection, geometric refinement, network disruption, matrix response and interface state can an experimental result be converted into a transferable design rule and its hidden microstructural cost be identified.

Table 1. Typical effects and potential penalties of major control routes.

Route	Primary Target	Typical Beneficial Change	Potential Adverse Change
Mn modification [72,116,117]	Phase identity, morphology, size and phase fraction	Suppresses high-aspect-ratio plates and promotes Chinese-script or compact phases	May increase α-Al(Fe,Mn)Si-type or coarse sludge phases and consume Si
Cr modification [108,154]	Phase identity, morphology and coarse particles	Stabilises selected low-aspect-ratio Fe-rich phases	High Cr/Mn can promote coarse sludge
Sr modification [120,121,124]	Eutectic Si, interfacial environment and Fe-rich morphology	Can shorten plates and alter local damage environments	May increase porosity or oxidation and has alloy-dependent effects

Table 1. *Cont.*

Route	Primary Target	Typical Beneficial Change	Potential Adverse Change
B-Ti inoculation [125,126,142]	Heterogeneous nucleation and particle number density	Raises nucleation density and can reduce the hazardous size tail	Can increase particle number, agglomeration or competing phase formation
Rare-earth additions [92,127–129,134]	Interfacial energy, local chemistry and morphology	Can refine or compact Fe-rich intermetallics	May form coarse rare-earth-bearing compounds or consume solute
Rapid cooling [56,72,75]	Size tail, morphology and three-dimensional networks	Restricts growth and compresses coarse particles and network scale	Can alter metastable phase selection without reducing total phase fraction
Ultrasound, electromagnetic stirring or high shear [111,113,114,144,146,149]	Nucleation, growth, spatial distribution and total phase population	Increases nucleation, perturbs growth and homogenises spatial distribution	Can increase particle number, local clustering or entrained inclusions
Homogenisation or solution treatment [27–29,112]	Phase transformation, size, solute and matrix state	Fragments or transforms β-Al-Fe-Si-type phases and redistributes solute	Excess treatment can coarsen phases or deplete strengthening solute
Extrusion, rolling or friction-stir processing [151]	Coarse particles, connected networks, grains and interfaces	Fragments coarse phases, severs networks and refines grains	May pre-crack particles, create bands or change interface integrity
Solid-state recycling [95–98,101]	Coarse particles, networks, chip boundaries and matrix	Avoids resolidification coarsening; shear-based routes also fragment inherited particles	Insufficient chip-boundary bonding reduces interface integrity

6. Multi-Impurity Coupling and Crossover Alloy Design

Fe rarely varies independently in real scrap. Si, Cu, Zn, Mn, Mg, Cr and trace elements jointly determine phase selection, solute partitioning and matrix strengthening, so single-factor claims that one element is beneficial for Fe can fail in a multi-impurity background [16,17,24,33,34,50,55,61,63–65,74,75,108,155]. The central task is not to add the effects of individual elements, but to trace how their coupling changes phase identity, particle scale and spatial distribution, and then alters matrix strengthening and local damage [24,34,55,108,155].

Fe-Si coupling is the clearest example. Si participates in β-Al-Fe-Si and α-Al(Fe,Mn)Si-type Fe-rich phases and controls their stability, but is also the central solute resource for precipitation strengthening in 6xxx alloys [16,32–34,50]. Additional Fe can increase the number and volume fraction of intermetallics, promote local networking and simultaneously consume matrix Si, thereby weakening β″ precipitation. The recycled-AA6016 result should not therefore be reduced to more particles causing lower ductility. The complete transfer path is that Fe changes particle population and spatial state while reducing the Si available for precipitation, thereby rebalancing particle-related damage and matrix strengthening [34].

Fe-Mn-Cr coupling presents a different trade-off. Mn/Cr can suppress high-aspect-ratio β-Al-Fe-Si phases and produce more compact morphologies, but may also generate a larger population of α-Al(Fe,Mn,Cr)Si or coarse sludge particles, increasing phase fraction or the hazardous size tail. Relative to the corresponding Mn-free alloys, 0.5 wt.% Mn reduced the maximum platelet size at the cast centre by 60.3% in the near-eutectic Al-11Si-2Fe alloy and by 81.3% in the far-from-eutectic Al-7Si-2Fe alloy [12]. Figure 14a,b

shows the residual microstructures after this modification rather than an unmodified-versus-modified pair. The near-eutectic alloy retains coarse platelet and polyhedral phases, whereas the far-from-eutectic alloy contains much shorter platelets together with a highly branched Chinese-script constituent and neighbouring polyhedral particles. The phase map in Figure 14c confirms this phase-specific juxtaposition. Mn has therefore reduced the dominant large-plate risk and reorganised the microstructure, but it has not eliminated branching, clustering or possible short-range linkage paths. The mechanical response is consistent with this balance: the far-from-eutectic alloy reaches a mean ultimate tensile strength of 141 ± 10 MPa and fracture elongation of 1.9 ± 0.6%, compared with 82 ± 13 MPa and 0.3 ± 0.2% for the near-eutectic alloy (Figure 14d) [12]. Similar results in recycled Al-9Si-1Fe show that a compact polygonal morphology can be offset by greater phase fraction or reduced interparticle spacing [108]. Conversely, a coordinated Mn/Cr/Sr/Ce design produced predominantly α-Al(Fe,Mn)Si at about 0.5–0.6 wt.% Fe and, after T7 treatment, approximately 220 MPa ultimate tensile strength and 13% elongation [156]. These results support multi-element expansion of the usable domain, but not a fixed universally applicable recipe.

Fe-Cu coupling is strongly alloy dependent. In Al-Si-Cu cast alloys, coarse Al_7Cu_2Fe can co-segregate with Al_2Cu and porosity in interdendritic regions, so particle geometry and spatial proximity directly participate in damage [43,54,55,62]. In age-hardenable wrought 2xxx and 7xxx alloys, coarse Fe-Cu-bearing particles also immobilise Cu and change the solute reservoir available for S- or η-type strengthening pathways. Although the detailed mechanisms differ, both classes require the Fe effect to be separated into particle geometry, phase partitioning and matrix strengthening rather than attributed to Fe embrittlement alone [24,54,55,62].

Zn and Mg extend the problem into crossover alloy design. AlMgZn(Cu) crossover alloys do not attempt to return scrap to conventional 5xxx, 6xxx or 7xxx compositions; they use the Zn, Mg, Cu and Fe already present in the feedstock to select new transformation pathways. Que et al. recently extended this concept to a mixed recycled wrought-aluminium composition and used modified $Al_3(Sc,Ti)$ precipitation to improve impurity tolerance in a multi-element matrix [157]. Samberger et al. found that Fe/Si ratio and cooling rate jointly control transformation from $Al_6(Fe,Mn)$ to $Al_{13}(Fe,Mn)_4$ or Al(Fe,Mn)Si-type phases. Cooling at about 60 K/s favoured smaller, more spheroidal particles; at about 1 K/s, coarsening was stronger; and the intermediate-rate regime was more sensitive to Fe/Si ratio [155]. Fe/Si ratio and cooling rate are therefore coupled variables that jointly determine phase identity, particle geometry and solute partitioning.

Synthesising the available evidence, we propose expressing multi-impurity tolerance as an uncertain feasibility domain rather than a point composition. Fe, Si, Cu and Zn in the feedstock have distributions with means, variances and correlations. The process objective is to identify combinations of Mn/Cr compensation, cooling rate and heat treatment that yield acceptable second-phase structures and mechanical properties for most batches. This domain must be product specific: automotive sheet prioritises yield strength, uniform elongation and bendability; structural castings prioritise yield strength, total elongation and fatigue; and extrusions additionally require control of surface defects and anisotropy. Crossover alloy design thus becomes a joint optimisation of the scrap probability distribution and a robust processing interval.

7. Data-Driven and Computation-Assisted Tolerance Design

Once the variables include Fe, Mn, Si, Cu, Zn, Mg, Cr, cooling rate, homogenisation and ageing, exhaustive experimentation becomes impractical. CALPHAD, solidification-kinetics models and machine learning are valuable not as substitutes for experiments, but

as a hierarchy for compressing the search space [12,31,50,126,154,158–162]. Thermodynamics first excludes clearly infeasible regions; kinetic and microstructural models then predict phase selection and scale; finally, experiments and data-driven methods establish microstructure-property relations [12,31,50,126,154,158–162]. Jarren et al. illustrate the screening potential of this hierarchy: a random-forest model trained on phase fractions from 4999 Thermo-Calc compositions enabled evaluation of more than 20 million Fe-Mn-Cu combinations in secondary $AlSi_7Mg_{0.3}$ [163].

7.1. CALPHAD: Thermodynamic and Non-Equilibrium Solidification-Path Screening

CALPHAD can do more than rank stable phases. Equilibrium sections define phase-stability regions and transformation temperatures, whereas Scheil-Gulliver calculations provide a thermodynamic baseline for the order of phase appearance, residual-liquid enrichment and phase fraction as a function of temperature [12,31,50,81,82,154]. In multicomponent Fe-Si-Cu-Zn-Mn alloys, metastable-phase suppression and composition-sensitivity calculations can expose competing solidification paths and identify narrow windows in which changes in the Si/Mn balance alter the first Fe-rich phase. Zhang et al. used CALPHAD to screen Cr/Mn combinations that stabilised α-$Al_{15}(Fe,Mn,Cr)_3Si_2$-type phases and suppressed high-risk Fe-bearing phases, followed by wedge-casting validation of the as-cast constitution and the tendency to form coarse sludge [154]. Mohammed et al. combined non-equilibrium solidification paths, precipitation driving forces and interfacial-energy estimates to explain why additional Mn can be beneficial, redundant or adverse depending on Fe level, Si content and thermal history [12].

Figure 6b also shows why a Scheil result must not be read as a direct cooling-rate prediction: measured intermetallic fractions depart from the simple Scheil trajectory and depend on holding time. Conventional Scheil calculations do not contain cooling rate explicitly and omit rate-dependent nucleation, partial back diffusion, diffusion-controlled peritectic transformations, melt flow and particle collision. These effects require coupling CALPHAD with nucleation and solidification-kinetics models, or calibration against in situ and casting experiments [12,56,72,73]. Thermodynamic and Scheil calculations remain powerful for screening phase sequences, transformation windows and phase fractions, but database uncertainty and extrapolation become more consequential in Fe-Si-Cu-Zn-Mn composition space. They also cannot directly predict the hazardous size tail, shape anisotropy or three-dimensional connectivity. Particle scale and spatial topology must therefore be supplied by kinetic models and experimental three-dimensional measurements rather than inferred from phase stability alone.

7.2. Machine Learning: Physically Constrained, High-Dimensional Microstructure-Property Mapping

Machine learning can represent high-dimensional nonlinear relations; however, the input variables determine what the model can learn [158–165]. A model that receives only Fe, Mn, Si and heat treatment and predicts ultimate tensile strength or elongation mainly captures average statistical associations. When the same Fe content produces different particle scales and connected states, those microstructural differences enter the residual noise. In a recycled Al-rare-earth dataset, Li et al. compared a back-propagation neural network, extreme learning machine, support-vector machine and random forest. Predictions improved when second-phase fractions were added to composition, and the random forest performed best. A candidate containing approximately 0.10 wt.% Sc was then validated by XCT, which resolved changes in Fe-rich phases and microporosity; ultimate tensile strength increased by about 4.37% [158]. This case shows that data-driven design becomes materially interpretable only when microstructure enters the input space. Recent work also explores multi-objective machine-learning design of Al-Si alloys [164] and

universal machine-learning potentials for accelerating CALPHAD-based phase-diagram predictions [165].

More direct progress comes from using dynamic microstructural information as labels. Xiang et al. combined in situ synchrotron solidification with machine learning to identify the dynamic evolution of multiple Fe-rich intermetallics in a recycled alloy [126]. Li et al. integrated cooling rates of 15.77–75.25 °C s^{-1}, XCT and machine learning to predict changes in intermetallic scale and morphology [76]. Unlike composition–property models, these approaches receive phase identity, size and morphology explicitly instead of requiring the algorithm to infer hidden structure from composition.

7.3. Next Step: Introducing Three-Dimensional Microstructure into the Input Space

We recommend that a minimum data structure for impurity-tolerance design should contain five layers: feedstock composition distributions, processing history, phase identity and fraction, three-dimensional microstructure, and mechanical damage response. Each specimen should at least record Fe, Si, Mn, Cu, Zn and Mg; cooling rate or a defensible solidification-scale proxy; heat treatment and deformation history; β-Al-Fe-Si and α-Al(Fe,Mn)Si phase fractions; D50, D90 or D95, maximum Feret diameter, aspect ratio and three-dimensional connectivity; and yield strength, ultimate tensile strength, uniform elongation and total elongation. Where possible, datasets should also include the strain evolution of particle-cracking fraction, interface-decohesion fraction and void volume fraction, together with fatigue and fracture measures.

A hierarchical data-fusion architecture is preferable to placing all variables directly into one black-box model:

Scrap composition and processing > phase selection and phase fraction > particle size, morphology, three-dimensional connectivity, matrix and interface state > damage probability and mechanical properties.

We propose this hierarchy for three reasons. First, prediction error can be localised to phase selection, microstructural scale or damage mapping rather than remaining an uninterpretable residual. Second, models become easier to transfer between processes: a new route requires recalibration of its effect on key microstructural features, not relearning of the entire composition–property relation. Third, uncertainty can propagate through a physical chain: feedstock variability first maps onto phase selection and microstructure, and ultimately produces a property distribution rather than a single deterministic value.

Figure 15 summarises the microstructure-based design logic developed in this review through representative phase morphologies, spatial particle arrangements and local damage mechanisms. It contrasts coarse, connected Fe-rich populations with refined, dispersed populations and distinguishes particle cracking, interface decohesion and void coalescence. Alloying, solidification control, heat treatment and deformation act on different parts of this microstructure-matrix-interface system. The favourable state is therefore not defined by particle refinement alone, but by a compatible combination of phase constitution, particle scale and connectivity, matrix load-bearing capacity and interface integrity. This synthesis supports product-specific impurity-tolerance windows rather than an alloy-independent maximum Fe content.

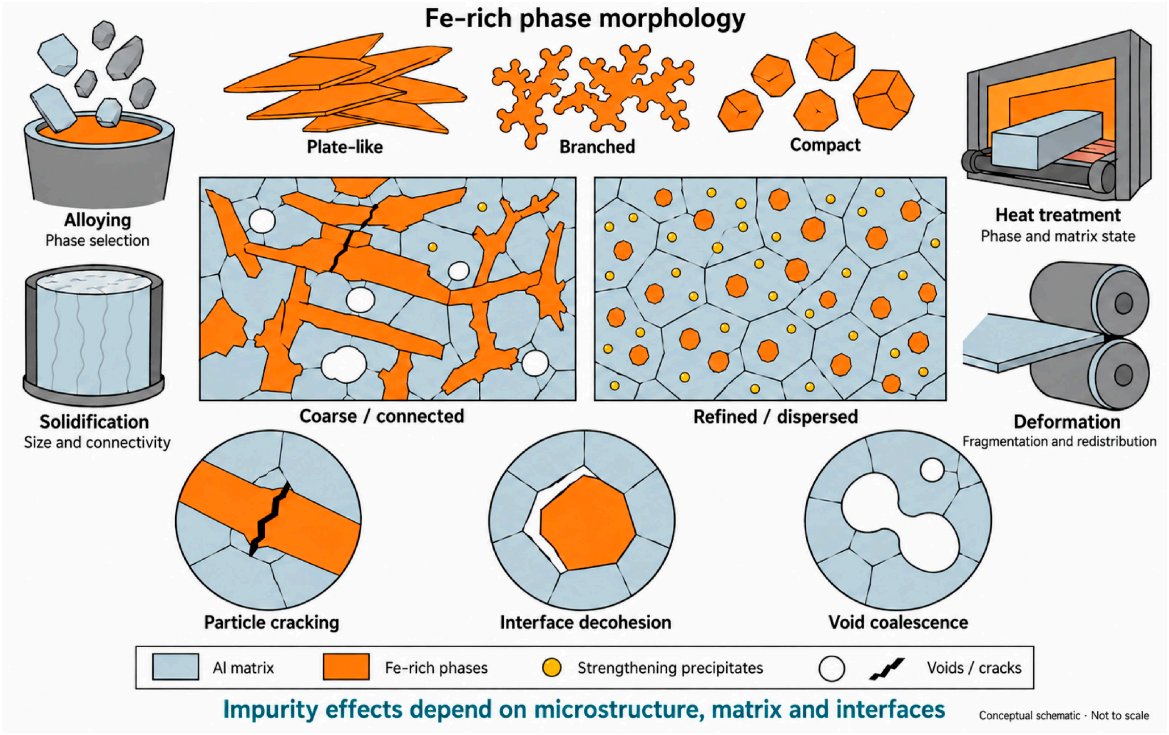


Figure 15. Conceptual schematic illustrating how Fe-rich phase morphology and distribution, matrix state and interface integrity govern impurity tolerance and damage in recycled aluminium alloys.

8. Conclusions and Outlook

8.1. Conclusions

1. Composition flags risk; microstructure determines tolerance. Fe content remains a useful feedstock-screening variable, but equal Fe levels can generate different phase identities, size distributions, morphologies and three-dimensional topologies and can redistribute Si, Cu and Mn. The resulting property response is therefore conditional on alloy system and processing route.
2. Phase identity is not a damage criterion. The heuristic that β-Al-Fe-Si is harmful and α-Al(Fe,Mn)Si is beneficial must give way to three-dimensional descriptors. Plate-like morphology, an enlarged hazardous size tail and greater connectivity usually increase risk, but compact or Chinese-script phases can still reduce ductility when phase fraction, clustering or interface condition is unfavourable.
3. Strength tolerance does not guarantee damage tolerance. The transition from load-bearing particle to dominant damage source is governed jointly by the hazardous size tail, local curvature, three-dimensional connectivity, phase fraction, matrix strength and interface integrity. No single particle-size or aspect-ratio threshold is therefore transferable across alloy systems.
4. Effective control must target the dominant microstructural bottleneck. Alloying changes phase selection and interfacial chemistry; cooling rate, ultrasound and external fields control particle scale and connectivity; homogenisation changes phase partitioning and matrix state; and deformation or solid-state recycling fragments particles and severs networks. Final ductility still depends on particle pre-cracking and interface or chip-boundary bonding, so mean particle length alone cannot demonstrate successful modification.
5. Multi-impurity design requires feasibility domains rather than single-element optima. Fe-Si coupling affects both Fe-rich phases and precipitation strengthening; Fe-Mn-Cr couples morphological refinement to possible increases in phase fraction or

sludge; and Fe-Cu acts through both coarse-particle damage and age-hardening solute. Crossover alloys are valuable because they use the composition already present in scrap to select workable phase pathways.

6. Predictive tolerance design requires a thermodynamics-kinetics-microstructure hierarchy. CALPHAD constrains phase sequences and feasibility windows; kinetic and in situ methods resolve pathway selection; XCT supplies size and connectivity descriptors; and machine learning approximates high-dimensional microstructure-property relations. Models become mechanistically useful only when particle-size distributions, three-dimensional connectivity and matrix state enter as inputs or intermediate variables.

8.2. Outlook

We identify standardisation of three-dimensional microstructural statistics as a priority so that tolerance criteria can be compared across studies. Reproducible definitions are needed for D50, D90/D95, maximum Feret diameter, aspect ratio, maximum connected volume, connected fraction, skeleton length and interparticle spacing, together with an explicit range over which two-dimensional proxies remain valid. Where routine XCT is impractical, a tiered strategy combining large-sample two-dimensional statistics with limited three-dimensional calibration is more realistic than making tomography a prerequisite for all industrial studies.

We identify the need for a quantitative matrix-strength-particle-state-damage map. Existing studies often report yield or ultimate tensile strength, mean particle size and fracture morphology separately, but rarely combine matrix flow stress, particle-size distribution, morphology, three-dimensional connectivity and cracking probability in the same specimen. HRDIC, in situ scanning-electron-microscope tension, synchrotron loading and inverse finite-element analysis can identify probabilistic damage-transition boundaries for different matrix and interface states.

We identify the dominance of monotonic-tension evidence as a major limitation. Fatigue, plane-strain fracture toughness, J-integral resistance, fatigue-crack-growth threshold, bendability and crash-energy absorption are needed to test whether strength tolerance separates from damage tolerance [46–48,80,93,102–106]. Relative to volume-averaged load bearing, these properties are more sensitive to failure boundaries governed by the hazardous size tail and connected three-dimensional defects.

We propose that engineering implementation should move from fixed composition points to probabilistic feedstock windows. Both scrap composition and processing conditions fluctuate as distributions [5,6,10,11]. The design question is therefore which alloying and process combinations produce safe second-phase size, morphology and spatial state with sufficiently high probability for a specified Fe-Si-Cu-Zn-Mn distribution while meeting strength, ductility and damage requirements. High-value recycling will then depend less on indefinitely increasing sorting purity and more on deliberately adapting material systems to unavoidable impurities through composition-process feasibility domains that can be calibrated continuously by experiment.

Author Contributions: D.Y.: Conceptualisation, Methodology, Investigation, Data Curation, Visualisation, Writing—Original Draft, Writing—Review and Editing. H.W.: Investigation, Resources, Validation, Writing—Review and Editing. H.L.: Investigation, Data Curation, Validation, Writing—Review and Editing. H.Z.: Investigation, Resources, Validation. Z.Y.: Investigation, Data Curation, Validation. X.L.: Data Curation, Writing—Original Draft. All authors have read and agreed to the published version of the manuscript.

Funding: This work was supported by the Independent Research and Development Scientific and Technological Project GJYF26-02 of Shandong Power Industry Boiler and Pressure Vessel Inspection Center Co., Ltd.

Data Availability Statement: No new experimental datasets were generated for this review. The underlying data are available from the cited studies, subject to their stated access conditions.

Conflicts of Interest: Author Dongxu Yang, Huafeng Wei, Haozhe Li, Hongwu Zhang and Zengwu Yue Shandong were employed by the company Power Industry Boiler & Pressure Vessel Inspection Center Co. Ltd. The remaining authors declare that the research was conducted in the absence of any commercial or financial relationships that could be construed as a potential conflict of interest.

References

1. Raabe, D.; Ponge, D.; Uggowitzer, P.J.; Roscher, M.; Paolantonio, M.; Liu, C.; Antrekowitsch, H.; Kozeschnik, E.; Seidmann, D.; Gault, B.; et al. Making sustainable aluminum by recycling scrap: The science of "dirty" alloys. *Prog. Mater. Sci.* **2022**, *128*, 100947. [CrossRef]
2. Raabe, D.; Tasan, C.C.; Olivetti, E.A. Strategies for improving the sustainability of structural metals. *Nature* **2019**, *575*, 64–74. [CrossRef] [PubMed]
3. Capuzzi, S.; Timelli, G. Preparation and melting of scrap in aluminum recycling: A review. *Metals* **2018**, *8*, 249. [CrossRef]
4. Gaustad, G.; Olivetti, E.; Kirchain, R. Improving aluminum recycling: A survey of sorting and impurity removal technologies. *Resour. Conserv. Recycl.* **2012**, *58*, 79–87. [CrossRef]
5. Hatayama, H.; Daigo, I.; Matsuno, Y.; Adachi, Y. Evolution of aluminum recycling initiated by the introduction of next-generation vehicles and scrap sorting technology, Resources. *Conserv. Recycl.* **2012**, *66*, 8–14. [CrossRef]
6. Rolseth, A.; Carlson, M.; Ghassemali, E.; Caro, L.P.; Jarfors, A.E.W. Impact of functional integration and electrification on aluminium scrap in the automotive sector: A review, Resources. *Conserv. Recycl.* **2024**, *205*, 107532. [CrossRef]
7. Paraskevas, D.; Kellens, K.; Dewulf, W.; Duflou, J.R. Environmental modelling of aluminium recycling: A Life Cycle Assessment tool for sustainable metal management. *J. Clean. Prod.* **2015**, *105*, 357–370. [CrossRef]
8. Kotadia, H.R.; Bareker, N.; Khan, M.H.; Ahuir-Torres, J.I.; Das, A. Aluminium recycling: A critical review of iron-bearing intermetallics in aluminium alloys. *Mater. Today Sustain.* **2025**, *30*, 101119. [CrossRef]
9. Wang, X.; Jiang, J.; Li, X.; Zeng, J.; Song, Q.; Jin, H. Fe impurity control in secondary aluminum alloys: A critical review of purification and upcycling. *Mater. Des.* **2026**, *268*, 116438. [CrossRef]
10. Efe, M.; Rohatgi, A.; Dai, Q.; Stapleton, B.; Rader, K.; Lipson, A.L.; Spangenberger, J.S. Alloy selective optical sorting of mixed post-consumer aluminum scrap streams, Resources. *Conserv. Recycl.* **2025**, *223*, 108500. [CrossRef]
11. Du, S.; Zhang, S.; Wang, J.; Lv, Z.; Xu, Z.; Liu, C.; Liu, J.; Liu, B. Energy flow of aerospace aluminum scraps cycle and advanced integration principles for upcycling technologies: A review. *J. Clean. Prod.* **2024**, *448*, 141176. [CrossRef]
12. Mohammed, W.; Chen, X.; Ponge, D.; Raabe, D. Thermodynamics-guided design of sustainable secondary Al-Si alloys for enhanced Fe-impurity tolerance and optimized Mn doping. *Acta Mater.* **2025**, *289*, 120932. [CrossRef]
13. Zhang, L.; Gao, J.; Damoah, L.N.W.; Robertson, D.G. Removal of iron from aluminum: A review. *Miner. Process. Extr. Metall. Rev.* **2012**, *33*, 99–157. [CrossRef]
14. Taylor, J.A. Iron-containing intermetallic phases in Al-Si based casting alloys. *Procedia Mater. Sci.* **2012**, *1*, 19–33. [CrossRef]
15. Cao, X.; Campbell, J. Morphology of β-Al5FeSi Phase in Al-Si Cast Alloys. *Mater. Trans.* **2006**, *47*, 1303–1312. [CrossRef]
16. Österreicher, J.A.; Arnoldt, A.R.; Gneiger, S.; Kunschert, G. Tolerance of Al-Mg-Si Wrought Alloys for High Fe Contents: The Role of Effective Si. *Metall. Mater. Trans. A* **2023**, *54*, 4472–4480. [CrossRef]
17. Pranav, K.J.; Sibi, S.P.; Jana, P.P. Evolution of Fe-rich intermetallic phases in cast and wrought aluminium alloys: Microstructural insights and property correlations. *J. Alloys Compd.* **2025**, *1042*, 184101. [CrossRef]
18. Ashtari, P.; Tetley-Gerard, K.; Sadayappan, K. Removal of iron from recycled aluminium alloys. *Can. Metall. Q.* **2012**, *51*, 75–80. [CrossRef]
19. de Moraes, H.L.; de Oliveira, J.R.; Espinosa, D.C.R.; Tenório, J.A.S. Removal of iron from molten recycled aluminum through intermediate phase filtration. *Mater. Trans.* **2006**, *47*, 1731–1736. [CrossRef]
20. Al-Helal, K.; Lazaro-Nebreda, J.; Patel, J.B.; Scamans, G.M. High-Shear De-Gassing and De-Ironing of an Aluminum Casting Alloy Made Directly from Aluminum End-of-Life Vehicle Scrap. *Recycling* **2021**, *6*, 66. [CrossRef]
21. Crepeau, P.N. Effect of iron in Al-Si casting alloys: A critical review. *Trans. Am. Foundrymen's Soc.* **1995**, *103*, 361–366.
22. Verma, A.; Kumar, S.; Grant, P.S.; O'Reilly, K.A.Q. Influence of cooling rate on the Fe intermetallic formation in an AA6063 Al alloy. *J. Alloys Compd.* **2013**, *555*, 274–282. [CrossRef]

23. Al-Helal, K.; Patel, J.B.; Fan, Z. Fe-Rich Intermetallic Formation and Mechanical Properties of Recycled AA6111 Alloy Strips Produced by Melt Conditioning Twin Roll Casting. *JOM* **2020**, *72*, 3753–3759. [CrossRef]
24. Kuijpers, N.C.W.; Vermolen, F.J.; Vuik, C.; Koenis, P.T.G.; Nilsen, K.E.; Zwaag, S.v.D. The dependence of the β-AlFeSi to α-Al(FeMn)Si transformation kinetics in Al-Mg-Si alloys on the alloying elements. *Mater. Sci. Eng. A* **2005**, *394*, 9–19. [CrossRef]
25. Avalos, A.G.; Torres, J.T.; Flores Valdés, F. Effect of the Fe/Mn ratio on the microstructural evolution of the AA6063 alloy with homogenization heat treatment interruption. *Metals* **2024**, *14*, 373. [CrossRef]
26. Kumar, S.; Grant, P.S.; O'Reilly, K.A.Q. Evolution of Fe bearing intermetallics during DC casting and homogenization of an Al-Mg-Si Al alloy. *Metall. Mater. Trans.* **2016**, *47*, 3000–3014. [CrossRef]
27. Alvarez-Antolin, F.; Asensio-Lozano, J.; Cofiño-Villar, A.; Gonzalez-Pociño, A. Analysis of Different Solution Treatments in the Transformation of β-AlFeSi Particles into α-(FeMn)Si and Their Influence on Different Ageing Treatments in Al-Mg-Si Alloys. *Metals* **2020**, *10*, 620. [CrossRef]
28. Li, Q.; Wang, J.; Liu, X.; Xue, C.; Wang, S.; Yang, X.; Tian, G.; Su, H.; Wu, X.; Miao, Y. Accelerating the dissolution and transformation of detrimental Fe-rich intermetallics in recycled Al-Mg-Si alloy by homogenization and hot deformation. *Mater. Charact.* **2024**, *213*, 114024. [CrossRef]
29. Kuijpers, N.C.W.; Vermolen, F.J.; Vuik, K.; van der Zwaag, S. A Model of the β-AlFeSi to α-Al(FeMn)Si Transformation in Al-Mg-Si Alloys. *Mater. Trans.* **2003**, *44*, 1448–1456. [CrossRef]
30. Bunkholt, S.; Nes, E.; Marthinsen, K. The effect of iron and the precipitation behavior of iron during annealing of a cold deformed commercial purity aluminium alloy. *Mater. Charact.* **2017**, *129*, 18–23. [CrossRef]
31. Sadeghi, I.; Wells, M.A.; Esmaeili, S. Modeling homogenization behavior of Al-Si-Cu-Mg aluminum alloy. *Mater. Des.* **2017**, *128*, 241–249. [CrossRef]
32. Qin, S.; Bendo, A.; Tsuchiya, T.; Lee, S.; Matsuda, K. Effect of cooling rate on precipitation during homogenization cooling in excess Si type Al-Mg-Si alloy. *Mater. Lett.* **2020**, *278*, 128363. [CrossRef]
33. Zhao, Q.; Qian, Z.; Cui, X.; Wu, Y.; Liu, X. Influences of Fe, Si and homogenization on electrical conductivity and mechanical properties of dilute Al-Mg-Si alloy. *J. Alloys Compd.* **2016**, *666*, 50–57. [CrossRef]
34. Duan, S.; Chen, L.; Huang, C.; Chen, W.; Tang, M.; Du, J. Role of iron content in microstructure-property relationships of sustainable secondary AA6016 alloy sheet. *Mater. Charact.* **2026**, *235*, 116252. [CrossRef]
35. Deng, Y.; Cao, Z.; Hu, D.; Smith, A.D.; Hunt, R.; Yan, K.; Robson, J.D. Insights into strain partitioning and void nucleation in recycled aluminium alloy: The role of Fe-rich intermetallic. *Mater. Sci. Eng. A* **2026**, *973*, 150757. [CrossRef]
36. Deng, Y.; Cao, Z.; Hunt, R.; Sun, W.; Zeng, G.; Shuai, S.; Robson, J.; Yan, K. Effects of increased Fe content on local damage in recycled 6xxx aluminium alloy. *Mater. Sci. Eng. A* **2025**, *943*, 148756. [CrossRef]
37. Zhou, L.; Wang, L.; Liu, S. In-situ investigation on β-Fe induced tensile fracture mechanism of A356 aluminium alloy. *Mater. Lett.* **2024**, *361*, 136073. [CrossRef]
38. Wang, X.; Zhao, H.; Xu, Q.; Han, Z. Tensile damage and fracture of high vacuum die-cast AlSiMgMn alloys with in-situ X-ray microtomography. *Mater. Sci. Eng. A* **2025**, *924*, 147869. [CrossRef]
39. Cinkilic, E.; Ridgeway, C.D.; Yan, X.; Luo, A.A. A formation map of iron-containing intermetallic phases in recycled cast aluminum alloys. *Metall. Mater. Trans.* **2019**, *50*, 5945–5956. [CrossRef]
40. Lazaro-Nebreda, J.; Patel, J.B.; Chang, I.T.H.; Stone, I.C.; Fan, Z. Solidification processing of scrap Al-alloys containing high levels of Fe. *IOP Conf. Ser. Mater. Sci. Eng.* **2019**, *529*, 012059. [CrossRef]
41. Duchaussoy, A.; Sauvage, X.; Edalati, K.; Horita, Z.; Renou, G.; Deschamps, A.; De Geuser, F. Structure and mechanical behavior of ultrafine-grained aluminum-iron alloy stabilized by nanoscaled intermetallic particles. *Acta Mater.* **2019**, *167*, 89–102. [CrossRef]
42. Que, Z.; Wang, Y.; Mendis, C.L.; Fang, C.; Xia, J.; Zhou, X.; Fan, Z. Understanding Fe- containing intermetallic compounds in Al alloys: An overview of recent advances from the LiME research hub. *Metals* **2022**, *12*, 1677. [CrossRef]
43. Li, X.-M.; Starink, M.J. Effect of compositional variations on characteristics of coarse intermetallic particles in overaged 7000 aluminium alloys. *Mater. Sci. Technol.* **2001**, *17*, 1324–1328. [CrossRef]
44. Hollingsworth, E.H.; Frank, G.R., Jr.; Willett, R.E. Identification of a new Al-Fe constituent, $FeAl_6$. *Trans. TMS-AIME* **1962**, *224*, 188–189.
45. Mathew, J.; Remy, G.; Williams, M.A.; Tang, F.; Srirangam, P. Effect of Fe Intermetallics on Microstructure and Properties of Al-7Si Alloys. *JOM* **2019**, *71*, 4362–4369. [CrossRef]
46. Yi, J.; Gao, Y.; Lee, P.; Lindley, T. Effect of Fe-content on fatigue crack initiation and propagation in a cast aluminum-silicon alloy (A356-T6). *Mater. Sci. Eng. A* **2004**, *386*, 396–407. [CrossRef]
47. Ceschini, L.; Boromei, I.; Morri, A.; Seifeddine, S.; Svensson, I.L. Effect of Fe content and microstructural features on the tensile and fatigue properties of the Al-Si10-Cu2 alloy. *Mater. Des. (1980–2015)* **2012**, *36*, 522–528. [CrossRef]
48. Závodská, D.; Kuchariková, L.; Tillová, E.; Guagliano, M.; Chalupová, M.; Uhríčik, M.; Belan, J. The effect of iron content on fatigue lifetime of AlZn10Si8Mg cast alloy. *Int. J. Fatigue* **2019**, *128*, 105189. [CrossRef]

49. Kim, D.; Kim, J.; Kobayashi, E. Microstructure characterization of rolled Al-Si-Mg-Fe alloy by three-dimensional tomography. *Mater. Sci. Eng. A* **2019**, *768*, 138449. [CrossRef]
50. Abou Khatwa, M.K.; Malakhov, D.V. On the thermodynamic stability of intermetallic phases in the AA6111 aluminum alloy. *Calphad* **2006**, *30*, 159–170. [CrossRef]
51. Khalifa, W.; Samuel, A.M.; Samuel, F.H.; Doty, H.W.; Valtierra, S. Metallographic observations of β-AlFeSi phase and its role in porosity formation in Al-7% Si alloys. *Int. J. Cast Met. Res.* **2006**, *19*, 156–166. [CrossRef]
52. Roy, N.; Samuel, A.M.; Samuel, F.H. Porosity formation in Al-9 Wt Pct Si-3 Wt Pct Cu alloy systems: Metallographic observations. *Metall. Mater. Trans.* **1996**, *27*, 415–429. [CrossRef]
53. Lu, L.; Dahle, A.K. Iron-rich intermetallic phases and their role in casting defect formation in hypoeutectic Al-Si alloys. *Metall. Mater. Trans.* **2005**, *36*, 819–835. [CrossRef]
54. Taylor, J.A.; Schaffer, G.B.; StJohn, D.H. The role of iron in the formation of porosity in Al-Si-Cu-based casting alloys: Part I. Initial experimental observations. *Metall. Mater. Trans.* **1999**, *30*, 1643–1650. [CrossRef]
55. Ma, Z.; Samuel, A.M.; Doty, H.W.; Valtierra, S.; Samuel, F.H. Effect of Fe content on the fracture behaviour of Al-Si-Cu cast alloys. *Mater. Des.* **2014**, *57*, 366–373. [CrossRef]
56. Que, Z.; Fang, C.; Fan, Z. Nucleation competition and phase transformation mechanisms in recycled aluminium alloys: Insights into θ-$Al_{13}Fe_4$, Al_6(Fe,Mn) and α-Al_{15}(Fe,Mn)$_3Si_2$. *J. Alloys Compd.* **2025**, *1032*, 181130. [CrossRef]
57. Feng, S.; Shearwood, M.; Lui, A.; Banks, D.; Nicholls, T.; Richards, S.; Wilson, M.D.; Grant, P.S.; Liotti, E. Probing the mechanisms of morphological evolution and phase selection of intermetallic compounds for impurity-tolerant processing of recycled Al alloys. *Acta Mater.* **2025**, *301*, 121591. [CrossRef]
58. Que, Z.; Wang, Y.; Fan, Z. Formation of the Fe-containing intermetallic compounds during solidification of Al-5Mg-2Si-0.7Mn-1.1Fe alloy. *Metall. Mater. Trans.* **2018**, *49*, 2173–2181. [CrossRef]
59. Wang, D.; Zhang, X.; Nagaumi, H.; Li, X.; Zhang, H. 3D morphology and growth mechanism of cubic α-Al(FeMnCr)Si intermetallic in an Al-Si cast alloy. *Mater. Lett.* **2020**, *277*, 128384. [CrossRef]
60. Lei, X.; Li, Y.; Du, X. Microstructural features of AlFeSi spherical particles in hypoeutectic Al-Si alloy. *Mater. Today Commun.* **2023**, *37*, 107105. [CrossRef]
61. Lin, B.; Zhang, W.; Zhao, Y.; Li, Y. Solid-state transformation of Fe-rich intermetallic phases in Al-5.0Cu-0.6Mn squeeze cast alloy with variable Fe contents during solution heat treatment. *Mater. Charact.* **2015**, *104*, 124–131. [CrossRef]
62. Hwang, J.Y.; Doty, H.W.; Kaufman, M.J. Crystallographic studies on the iron-containing intermetallic phases in the 319-type aluminium casting alloys. *Philos. Mag.* **2008**, *88*, 607–619. [CrossRef]
63. Liu, K.; Cao, X.; Chen, X.G. A New Iron-Rich Intermetallic-AlmFe Phase in Al-4.6Cu-0.5Fe Cast Alloy. *Metall. Mater. Trans. A* **2012**, *43*, 1097–1101. [CrossRef]
64. Jiang, B.; Ji, Z.S.; Xu, H.Y.; Hu, M.L.; Zhang, Y.B.; Wang, S.Z. Transformation of Fe-rich intermetallic phases and eutectic Si morphology in Al-Si-Cu-Fe cast alloy with solution treatment. *Mater. Res. Express* **2019**, *6*, 066515. [CrossRef]
65. García-García, G.; Espinoza-Cuadra, J.; Mancha-Molinar, H. Copper content and cooling rate effects over second phase particles behavior in industrial aluminum-silicon alloy 319. *Mater. Des.* **2007**, *28*, 428–433. [CrossRef]
66. Westengen, H. Formation of intermetallic compounds during DC-casting of a commercial purity Al-Fe-Si alloy. *Z. Fur Met.* **1982**, *73*, 360–368. [CrossRef]
67. Young, R.M.K.; Clyne, T.W. An Al-Fe intermetallic phase formed during controlled solidification. *Scr. Metall.* **1981**, *15*, 1211–1216. [CrossRef]
68. Puncreobutr, C.; Phillion, A.B.; Fife, J.L.; Rockett, P.; Horsfield, A.P.; Lee, P.D. In situ quantification of the nucleation and growth of Fe-rich intermetallics during Al alloy solidification. *Acta Mater.* **2014**, *79*, 292–303. [CrossRef]
69. Terzi, S.; Taylor, J.A.; Cho, Y.H.; Salvo, L.; Suéry, M.; Boller, E.; Dahle, A.K. In situ study of nucleation and growth of the irregular α-Al/β-Al5FeSi eutectic by 3-D synchrotron X-ray microtomography. *Acta Mater.* **2010**, *58*, 5370–5380. [CrossRef]
70. Gao, T.; Wu, Y.; Li, C.; Liu, X. Morphologies and growth mechanisms of α-Al(FeMn) Si in Al-Si-Fe-Mn alloy. *Mater. Lett.* **2013**, *110*, 191–194. [CrossRef]
71. Bjurenstedt, A.; Casari, D.; Seifeddine, S.; Mathiesen, R.H.; Dahle, A.K. In-situ study of morphology and growth of primary α-Al(FeMnCr)Si intermetallics in an Al-Si alloy. *Acta Mater.* **2017**, *130*, 1–9. [CrossRef]
72. Becker, H.; Bergh, T.; Vullum, P.E.; Leineweber, A.; Li, Y. Effect of Mn and cooling rates on α-, β- and δ-Al-Fe-Si intermetallic phase formation in a secondary Al-Si alloy. *Materialia* **2019**, *5*, 100198. [CrossRef]
73. Wang, J.; Lee, P.; Hamilton, R.; Li, M.; Allison, J. The kinetics of Fe-rich intermetallic formation in aluminium alloys: In situ observation. *Scr. Mater.* **2009**, *60*, 516–519. [CrossRef]
74. Zhang, Z.; Tezuka, H.; Kobayashi, E.; Sato, T. Effects of the Mn/Fe Ratio and Cooling Rate on the Modification of Fe Intermetallic Compounds in Cast A356 Based Alloy with Different Fe Contents. *Mater. Trans.* **2013**, *54*, 1484–1490. [CrossRef]
75. Saghafian, H.; Shabestari, S.G.; Ghadami, S.; Ghoncheh, M.H. Effects of Iron, Manganese, and Cooling Rate on Microstructure and Dry Sliding Wear Behavior of LM13 Aluminum Alloy. *Tribol. Trans.* **2017**, *60*, 888–901. [CrossRef]

76. Li, Q.; Wang, J.; Xue, C.; Miao, Y.; Hou, Q.; Meng, Y.; Yang, X.; Li, X. Quantifying the effects of cooling rates on Fe-rich intermetallics in recycled Al-Si-Cu alloys by machine learning. *J. Alloys Compd.* **2025**, *1014*, 178718. [CrossRef]
77. Yang, D.; Song, D.; Yang, D.; Zhao, Y.; Li, D.; Zhou, N.; Li, X.; Guo, Z.-Q. 3D characteristics of Fe-rich phase and its effect on mechanical properties of AA3104 alloys. *J. Mater. Res. Technol.* **2025**, *35*, 3634–3644. [CrossRef]
78. Yang, D.; Song, D.; Tang, C.; Zhao, Y.; Cai, Y.; Chen, J.; Zhang, Z.; Zhou, N.; Zhang, W. 3D morphological evolution of the Fe-rich phase and mechanical properties of the recyclable A356 alloy. *Mater. Today Commun.* **2024**, *41*, 110425. [CrossRef]
79. Cao, X.; Campbell, J. The nucleation of Fe-Rich phases on oxide films in Al-11.5Si- 0.4Mg cast alloys. *Metall. Mater. Trans.* **2003**, *34*, 1409–1420. [CrossRef]
80. Wagner, R.; Seleznev, M.; Fischer, H.; Ditscherlein, R.; Becker, H.; Dietrich, B.G.; Keßler, A.; Leißner, T.; Wolf, G.; Leineweber, A.; et al. Impact of melt conditioning and filtration on iron-rich β phase in AlSi9Cu3 and its fatigue life studied by µCT. *Mater. Charact.* **2021**, *174*, 111039. [CrossRef]
81. Andersson, J.O.; Helander, T.; Höglund, L.; Shi, P.; Sundman, B. Thermo-Calc & DICTRA, computational tools for materials science. *Calphad* **2002**, *26*, 273–312. [CrossRef]
82. Chen, H.-L.; Chen, Q.; Engström, A. Development and applications of the TCAL aluminum alloy database. *Calphad* **2018**, *62*, 154–171. [CrossRef]
83. Zhao, Y.; Zhang, W.; Song, D.; Lin, B.; Shen, F.; Zheng, D.; Xie, C.; Sun, Z.; Fu, Y.; Li, R. Nucleation and growth of Fe-rich phases in Al-5Ti-1B modified Al-Fe alloys investigated using synchrotron X-ray imaging and electron microscopy. *J. Mater. Sci. Technol.* **2021**, *80*, 84–99. [CrossRef]
84. Lui, A.; Grant, P.S.; Stone, I.C.; O'Reilly, K.A.Q. The role of grain refiner in the nucleation of AlFeSi intermetallic phases during solidification of a 6xxx aluminum alloy. *Metall. Mater. Trans.* **2019**, *50*, 5242–5252. [CrossRef]
85. Li, H.T.; Wang, Y.; Fan, Z. Mechanisms of enhanced heterogeneous nucleation during solidification in binary Al-Mg alloys. *Acta Mater.* **2012**, *60*, 1528–1537. [CrossRef]
86. Wang, W.; Takata, N.; Suzuki, A.; Kobashi, M.; Kato, M. Formation of multiple intermetallic phases in a hypereutectic Al-Fe binary alloy additively manufactured by laser powder bed fusion. *Intermetallics* **2020**, *125*, 106892. [CrossRef]
87. Que, Z.; Mendis, C.L. Formation of θ-Al13Fe4 and the multi-step phase transformations to α-Al8Fe2Si, β-Al5FeSi and δ-Al4FeSi2 in Al-20Si-0.7Fe alloy. *Intermetallics* **2020**, *127*, 106960. [CrossRef]
88. Yu, J.M.; Wanderka, N.; Rack, A.; Daudin, R.; Boller, E.; Markötter, H.; Manzoni, A.; Vogel, F.; Arlt, T.; Manke, I.; et al. Formation of intermetallic δ phase in Al- 10Si-0.3Fe alloy investigated by in-situ 4D X-ray synchrotron tomography. *Acta Mater.* **2017**, *129*, 194–202. [CrossRef]
89. Warmuzek, M.; Rabczak, K.; Sieniawski, J. The course of the peritectic transformation in the Al-rich Al-Fe-Mn-Si alloys. *J. Mater. Process. Technol.* **2005**, *162–163*, 422–428. [CrossRef]
90. Kumar, S.; O'Reilly, K.A.Q. Influence of Al grain structure on Fe bearing intermetallics during DC casting of an Al-Mg-Si alloy. *Mater. Char.* **2016**, *120*, 311–322. [CrossRef]
91. Bjurenstedt, A.; Ghassemali, E.; Seifeddine, S.; Dahle, A.K. The effect of Fe-rich intermetallics on crack initiation in cast aluminium: An in-situ tensile study. *Mater. Sci. Eng. A* **2019**, *756*, 502–507. [CrossRef]
92. Zheng, Q.; Zhang, L.; Jiang, H.; Zhao, J.; He, J. Effect mechanisms of micro-alloying element La on microstructure and mechanical properties of hypoeutectic Al-Si alloys. *J. Mater. Sci. Technol.* **2020**, *47*, 142–151. [CrossRef]
93. Zheng, H.; Jiang, Y.; Liu, F.; Zhao, H. Synergistic effect of externally solidified crystals and Fe-rich intermetallic on the fracture behavior of HPDC alloy. *J. Mater. Res. Technol.* **2023**, *27*, 2822–2832. [CrossRef]
94. Xu, D.; Zhu, C.; Xu, C.; Chen, K. Microstructures and tensile fracture behavior of 2219 wrought Al-Cu alloys with different impurity of Fe. *Metals* **2021**, *11*, 174. [CrossRef]
95. Wang, T.; Li, Z.; Liu, T.; Shukla, S.; Mukhopadhyay, A.; Li, X.; Grant, G.J. Influence of iron impurity on recycled aluminum alloy produced by friction extrusion. *Mater. Sci. Eng. A* **2026**, *960*, 150147. [CrossRef]
96. Güley, V.; Khalifa, N.B.; Tekkaya, A.E. Direct recycling of 1050 aluminum alloy scrap material mixed with 6060 aluminum alloy chips by hot extrusion. *Int. J. Mater. Form.* **2010**, *3*, 853–856. [CrossRef]
97. Paraskevas, D.; Vanmeensel, K.; Vleugels, J.; Dewulf, W.; Deng, Y.; Duflou, J. Spark Plasma Sintering As a Solid-State Recycling Technique: The Case of Aluminum Alloy Scrap Consolidation. *Materials* **2014**, *7*, 5664–5687. [CrossRef] [PubMed]
98. El Aal, M.I.A.; Taha, M.A.; Selmy, A.I.; El-Gohry, A.M.; Kim, H.S. Solid state recycling of aluminium AA6061 alloy chips by hot extrusion. *Mater. Res. Express* **2019**, *6*, 036525. [CrossRef]
99. Chiba, R.; Yoshimura, M. Solid-state recycling of aluminium alloy swarf into c-channel by hot extrusion. *J. Manuf. Process.* **2015**, *17*, 1–8. [CrossRef]
100. Fogagnolo, J.B.; Ruiz-Navas, E.M.; Simón, M.A.; Martinez, M.A. Recycling of aluminium alloy and aluminium matrix composite chips by pressing and hot extrusion. *J. Mater. Process. Technol.* **2003**, *143–144*, 792–795. [CrossRef]
101. Shamsudin, S.; Lajis, M.A.; Zhong, Z.W.; Ahmad, A.; Wagiman, A. Weld strength in solid-state recycling of aluminum chips. *Mater. Und Werkst.* **2017**, *48*, 290–298. [CrossRef]

102. Kuroki, Y.; Tanaka, T.; Sato, T.; Kamio, A. Effects of defects and Fe intermetallic compounds on fatigue properties of Al-Si-Cu-Mg alloy castings. *Mater. Trans.* **2001**, *42*, 2339–2344. [CrossRef]
103. Lassance, D.; Fabregue, D.; Delannay, F.; Pardoen, T. Micromechanics of room and high temperature fracture in 6xxx Al alloys. *Prog. Mater. Sci.* **2007**, *52*, 62–129. [CrossRef]
104. Ceschini, L.; Boromei, I.; Morri, A.; Seifeddine, S.; Svensson, I.L. Microstructure, tensile and fatigue properties of the Al-10% Si-2% Cu alloy with different Fe and Mn content cast under controlled conditions. *J. Mater. Process. Technol.* **2009**, *209*, 5669–5679. [CrossRef]
105. Luo, A.A.; Kubic, R.C.; Tartaglia, J.M. Microstructure and fatigue properties of hydroformed aluminum alloys 6063 and 5754. *Metall. Mater. Trans. A* **2003**, *34*, 2549–2557. [CrossRef]
106. Kucharikova, L.; Medvecka, D.; Tillova, E.; Belan, J.; Kritikos, M.; Chalupova, M.; Uhríc, M. The effect of the β-Al5FeSi phases on microstructure, mechanical and fatigue properties in A356.0 cast alloys with higher Fe content without additional alloying of Mn. *Materials* **2021**, *14*, 1943. [CrossRef] [PubMed]
107. Blind, J.A.; Martin, J.W. The effect of dispersoids on the ductile fracture toughness of Al Mg Si alloys. *Mater. Sci. Eng.* **1983**, *57*, 49–54. [CrossRef]
108. Balasubramani, N.; Moodispaw, M.; Luo, A.A. Controlling the Fe-intermetallic phases and mechanical properties of secondary Al-9Si-1Fe alloy with Cr and Mn additions. *J. Mater. Sci. Technol.* **2025**, *206*, 135–152. [CrossRef]
109. Song, D.; Zhao, Y.; Wang, Z.; Jia, Y.; Huang, H.; Zhang, D.; Zhang, W. Effect of Mn/Fe ratio on Fe removal efficiency and tensile ductility of an Al-7.0Si-2.4Fe alloy. *J. Mater. Res.* **2021**, *36*, 1357–1366. [CrossRef]
110. Chanyathunyaroj, K.; Patakham, U.; Kou, S.; Limmaneevichitr, C. Mechanical properties of squeeze-cast Al-7Si-0.3Mg alloys with Sc-modified Fe-rich intermetallic compounds. *Rare Met.* **2018**, *37*, 769–777. [CrossRef]
111. Zhang, Z.; Li, Q.; Wang, K.; Hu, P. Effects of ultrasonic treatment on microstructure and mechanical properties of recycled Al-9Si-1Fe alloy. *Int. J. Met.* **2025**, *19*, 2711–2723. [CrossRef]
112. Villeneuve, C.; Samuel, F.H. Fragmentation and dissolution of β-Al5FeSi phase during solution heat treatment of Al-13wt% Si-Fe alloys. *Int. J. Cast Met. Res.* **1999**, *12*, 145–160. [CrossRef]
113. Zhong, G.; Wu, S.; Jiang, H.; An, P. Effects of ultrasonic vibration on the iron-containing intermetallic compounds of high silicon aluminum alloy with 2% Fe. *J. Alloys Compd.* **2010**, *492*, 482–487. [CrossRef]
114. Khalifa, W.; Tsunekawa, Y.; Okumiya, M. Effect of ultrasonic treatment on the Fe-intermetallic phases in ADC12 die cast alloy. *J. Mater. Process. Technol.* **2010**, *210*, 2178–2187. [CrossRef]
115. Zhang, Y.; Jie, J.; Gao, Y.; Lu, Y.; Li, T. Effects of ultrasonic treatment on the formation of iron-containing intermetallic compounds in Al-12%Si-2%Fe alloys. *Intermetallics* **2013**, *42*, 120–125. [CrossRef]
116. Wang, B.; Wang, J.; Liu, X.; Li, Q.; Liu, X. Uncovering the effects of neutralizing elements (Co, Mn and Cr) on the Fe-rich intermetallic formation in Al-Si-Cu alloys. *Mater. Sci. Eng. A* **2022**, *858*, 144090. [CrossRef]
117. Song, D.; Zhao, Y.; Jia, Y.; Li, R.; Zhou, N.; Zheng, K.; Fu, Y.; Zhang, W. Study of the evolution mechanisms of Fe-rich phases in Al-Si-Fe alloys with Mn modification using synchrotron X-ray imaging. *J. Alloys Compd.* **2022**, *915*, 165378. [CrossRef]
118. Khan, M.H.; Das, A.; Li, Z.; Kotadia, H.R. Effects of Fe, Mn, chemical grain refinement and cooling rate on the evolution of Fe intermetallics in a model 6082 Al-alloy. *Intermetallics* **2021**, *132*, 107132. [CrossRef]
119. Shabestari, S.G. The effect of iron and manganese on the formation of intermetallic compounds in aluminum-silicon alloys. *Mater. Sci. Eng. A* **2004**, *383*, 289–298. [CrossRef]
120. Balasubramani, N.; Moodispaw, M.; Cinkilic, E.; Miao, J.; Luo, A.A. Strontium effects on the formation of iron-intermetallic phases in secondary Al-9Si-0.6Fe alloys. *Metall. Mater. Trans. A* **2024**, *55*, 550–568. [CrossRef]
121. Li, Q.; Wang, J.; Xue, C.; Miao, Y.; Hou, Q.; Yang, X.; Meng, Y.; Yang, Z.; Tian, G.; Su, H.; et al. Effects of Sr on Fe-rich intermetallics in recycled Al-Si-Cu alloys. *J. Mater. Sci.* **2024**, *59*, 11572–11595. [CrossRef]
122. Yu, J.M.; Wanderka, N.; Rack, A.; Daudin, R.; Boller, E.; Markötter, H.; Manzoni, A.; Vogel, F.; Arlt, T.; Manke, I.; et al. Influence of impurities, strontium addition and cooling rate on microstructure evolution in Al-10Si-0.3Fe casting alloys. *J. Alloys Compd.* **2018**, *766*, 818–827. [CrossRef]
123. Vandersluis, E.; Ravindran, C.; Sediako, D.; Elsayed, A.; Byczynski, G. Strontium-modification in the stepwise solidification of A319 Al alloy: An in-situ neutron diffraction study. *J. Alloys Compd.* **2019**, *792*, 240–249. [CrossRef]
124. Ashtari, P.; Tezuka, H.; Sato, T. Modification of Fe-containing intermetallic compounds by K addition to Fe-rich AA319 aluminum alloys. *Scr. Mater.* **2005**, *53*, 937–942. [CrossRef]
125. Song, D.; Zhao, Y.; Jia, Y.; Li, X.; Fu, Y.; Zhang, W. Synergistic effects of Mn and B on iron-rich intermetallic modification of recycled Al alloy. *J. Mater. Res. Technol.* **2023**, *24*, 527–541. [CrossRef]
126. Xiang, K.; Qin, L.; Zhao, Y.; Huang, S.; Du, W.; Boller, E.; Rack, A.; Li, M.; Mi, J. Operando study of the dynamic evolution of multiple Fe-rich intermetallics of an Al recycled alloy in solidification by synchrotron X-ray and machine learning. *Acta Mater.* **2024**, *279*, 120267. [CrossRef]

127. Zhao, B.; Xing, S.; Shan, A.; Yan, G.; Jiang, X. Influence of La addition on Fe-rich intermetallic phases formation and mechanical properties of Al-7Si-4Cu-0.35Mg- 0.2Fe alloys prepared by squeeze casting. *Intermetallics* **2023**, *153*, 107783. [CrossRef]
128. Wan, B.; Chen, W.; Liu, L.; Cao, X.; Zhou, L.; Fu, Z. Effect of trace yttrium addition on the microstructure and tensile properties of recycled Al-7Si-0.3 Mg-1.0 Fe casting alloys. *Mater. Sci. Eng. A* **2016**, *666*, 165–175. [CrossRef]
129. Song, D.; Zhao, Y.; Jia, Y.; Huang, G.; Zhang, Z.; Zhou, N.; Li, X.; Zheng, K.; Fu, Y.; Zhang, W. Effect of B addition on the formation of Fe-rich phases in Al-Si-Fe alloys. *J. Alloys Compd.* **2023**, *930*, 167426. [CrossRef]
130. Tang, Q.; Zhao, J.; Wang, T.; Chen, J.; He, K. The effects of neodymium addition on the intermetallic microstructure and mechanical properties of Al-7Si-0.3 Mg-0.3 Fe alloys. *J. Alloys Compd.* **2018**, *741*, 161–173. [CrossRef]
131. Zhao, B.; Xing, S.; Sun, H.; Yan, G.; Gao, W.; Ou, L. Effect of rare-earth La on microstructure and mechanical properties of Al7Si4CuMg alloys prepared by squeeze casting. *J. Mater. Sci.* **2022**, *57*, 12064–12083. [CrossRef]
132. Liang, Y.; Shi, Z.; Li, G.; Zhang, R.; Li, M. Effects of rare earth modification on microstructure refinement and mechanical properties of Al-2 wt% Fe alloys. *Mater. Res. Express* **2019**, *6*, 106504. [CrossRef]
133. Jiang, W.; Fan, Z.; Dai, Y.; Li, C. Effects of rare earth elements addition on microstructures, tensile properties and fractography of A357 alloy. *Mater. Sci. Eng. A* **2014**, *597*, 237–244. [CrossRef]
134. Fan, C.; Long, S.-Y.; Yang, H.-D.; Wang, X.-J.; Zhang, J.-C. Influence of Ce and Mn addition on α-Fe morphology in recycled Al-Si alloy ingots. *Int. J. Miner. Metall. Mater.* **2013**, *20*, 890–895. [CrossRef]
135. Beeri, O.; Dunand, D.C.; Seidman, D.N. Roles of impurities on precipitation kinetics of dilute Al-Sc alloys. *Mater. Sci. Eng. A* **2010**, *527*, 3501–3509. [CrossRef]
136. Seifeddine, S.; Johansson, S.; Svensson, I.L. The influence of cooling rate and manganese content on the β-Al5FeSi phase formation and mechanical properties of Al-Si-based alloys. *Mater. Sci. Eng. A* **2008**, *490*, 385–390. [CrossRef]
137. Kotadia, H.R.; Qian, M.; Das, A. Solidification of aluminium alloys under ultrasonication: An overview. *Trans. Indian Inst. Met.* **2018**, *71*, 2681–2686. [CrossRef]
138. Tonry, C.E.H.; Djambazov, G.; Dybalska, A.; Griffiths, W.D.; Beckwith, C.; Bojarevics, V.; Pericleous, K.A. Acoustic resonance for contactless ultrasonic cavitation in alloy melts. *Ultrason. Sonochem.* **2020**, *63*, 104959. [CrossRef] [PubMed]
139. Pericleous, K.; Bojarevics, V.; Djambazov, G.; Dybalska, A.; Griffiths, W.D.; Tonry, C. Contactless ultrasonic cavitation in alloy melts. *Materials* **2019**, *12*, 3610. [CrossRef] [PubMed]
140. Kotadia, H.R.; Qian, M.; Eskin, D.G.; Das, A. On the microstructural refinement in commercial purity Al and Al-10wt% Cu alloy under ultrasonication during solidification. *Mater. Des.* **2017**, *132*, 266–274. [CrossRef]
141. Das, A.; Kotadia, H.R. Effect of high-intensity ultrasonic irradiation on the modification of solidification microstructure in a Si-rich hypoeutectic Al-Si alloy. *Mater. Chem. Phys.* **2011**, *125*, 853–859. [CrossRef]
142. Khan, M.H.; Das, A.; Khan, T.I.; Li, Z.; Kotadia, H.R. Microstructural modification in an Al-Mg-Si (6082) alloy with high Fe content using inoculation and/or high- intensity ultrasonication. *J. Alloys Compd.* **2025**, *1012*, 178500. [CrossRef]
143. Li, Y.; Wang, Z.; Zhou, X.; Xiao, H.; Yue, Q. A review of electromagnetic stirring on solidification characteristics of molten metal in continuous casting. *Metall. Res. Technol.* **2024**, *121*, 312. [CrossRef]
144. Shiga, K.; Fujiwara, T.; Murakami, Y.; Omura, N. In situ X-ray imaging of α-Al (FeMn)Si grain evolution during solidification of an Al-Si alloy with electromagnetic stirring. *J. Alloys Compd.* **2024**, *1004*, 175866. [CrossRef]
145. Sree Manu, K.M.; Barekar, N.S.; Lazaro-Nebreda, J.; Patel, J.B.; Fan, Z. In-situ microstructural control of A6082 alloy to modify second phase particles by melt conditioned direct chill (MC-DC) casting process—A novel approach. *J. Mater. Process. Technol.* **2021**, *295*, 117170. [CrossRef]
146. Lazaro-Nebreda, J.; Patel, J.B.; Al-Helal, K.; Gao, F.; Stone, I.; Chang, I.T.H.; Scamans, G.M.; Fan, Z. De-ironing of aluminium alloy melts by high shear melt conditioning technology: An overview. *Metals* **2022**, *12*, 1579. [CrossRef]
147. Becker, H.; Thum, A.; Distl, B.; Kriegel, M.J.; Leineweber, A. Effect of melt conditioning on removal of Fe from secondary Al-Si alloys containing Mg, Mn, and Cr. *Metall. Mater. Trans. A* **2018**, *49*, 6375–6389. [CrossRef]
148. Kotadia, H.R.; Patel, J.B.; Li, H.T.; Gao, F.; Fan, Z. Microstructure evolution in melt conditioned direct chill (MC-DC) casting of Fe-rich Al-alloy. *Adv. Mater. Res.* **2014**, *1019*, 90–95. [CrossRef]
149. Kotadia, H.R.; Babu, N.H.; Zhang, H.; Arumuganathar, S.; Fan, Z. Solidification behavior of intensively sheared hypoeutectic Al-Si alloy liquid. *Metall. Mater. Trans. A* **2011**, *42*, 1117–1126. [CrossRef]
150. Abu-Dheir, N.; Khraisheh, M.; Saito, K.; Male, A. Silicon morphology modification in the eutectic Al-Si alloy using mechanical mold vibration. *Mater. Sci. Eng. A* **2005**, *393*, 109–117. [CrossRef]
151. Hannard, F.; Castin, S.; Maire, E.; Mokso, R.; Pardoen, T.; Simar, A. Ductilization of aluminium alloy 6056 by friction stir processing. *Acta Mater.* **2017**, *130*, 121–136. [CrossRef]
152. Xiao, Y.; Reuter, M.A. Recycling of distributed aluminium turning scrap. *Miner. Eng.* **2002**, *15*, 963–970. [CrossRef]
153. Mashhadi, H.A.; Moloodi, A.; Golestanipour, M.; Karimi, E.Z.V. Recycling of aluminium alloy turning scrap via cold pressing and melting with salt flux. *J. Mater. Process. Technol.* **2009**, *209*, 3138–3142. [CrossRef]

154. Zhang, C.; Luo, A.A.; Zhang, F. CALPHAD-guided suppression of detrimental Fe-containing phases in secondary aluminum alloys. *Calphad* **2025**, *89*, 102830. [CrossRef]
155. Samberger, S.; Weißensteiner, I.; Tunes, M.A.; Stemper, L.; Kainz, C.; Morak, R.; Uggowitzer, P.J.; Pogatscher, S. Impurity-induced phase transformations in AlMgZn(Cu) crossover alloys: Pathways to enhance recycling content and processability. *J. Manuf. Process.* **2025**, *150*, 1178–1193. [CrossRef]
156. Garcia, G.; Moodispaw, M.; Zhang, J.; Miao, J.; Luo, A.A. Developing Structural Die-Cast Alloys from Automotive Aluminum Scrap Materials. *Int. J. Met.* **2026**. [CrossRef]
157. Que, Z.; Negrea, R.F.; Fang, C. Development of sustainable mixed recycled wrought aluminium alloys with modified Al3(Sc,Ti) for improved impurity tolerance. *Mater. Today Sustain.* **2026**, *35*, 101395. [CrossRef]
158. Li, Q.; Wang, J.; Xue, C.; Miao, Y.; Hou, Q.; Meng, Y.; Yang, X.; Li, X. Design of high strength and ductile recycled Al alloys by machine learning. *Mater. Today Commun.* **2025**, *44*, 111929. [CrossRef]
159. Yi, W.; Liu, G.; Lu, Z.; Gao, J.; Zhang, L. Efficient alloy design of Sr-modified A356 alloys driven by computational thermodynamics and machine learning. *J. Mater. Sci. Technol.* **2022**, *112*, 277–290. [CrossRef]
160. Butler, K.T.; Davies, D.W.; Cartwright, H.; Isayev, O.; Walsh, A. Machine learning for molecular and materials science. *Nature* **2018**, *559*, 547–555. [CrossRef] [PubMed]
161. Ramprasad, R.; Batra, R.; Pilania, G.; Mannodi-Kanakkithodi, A.; Kim, C. Machine learning in materials informatics: Recent applications and prospects. *NPJ Comput. Mater.* **2017**, *3*, 54. [CrossRef]
162. Lookman, T.; Balachandran, P.V.; Xue, D.; Yuan, R. Active learning in materials science with emphasis on adaptive sampling using uncertainties for targeted design. *NPJ Comput. Mater.* **2019**, *5*, 21. [CrossRef]
163. Jarren, L.C.; Viardin, A.; Gazenbiller, E.; Apel, M.; Eiken, J.; Li, Q.; Zheludkevich, M.; Höche, D. Machine learning-accelerated CALPHAD analysis of impurity-driven intermetallic formation in secondary $AlSi_7Mg_{0.3}$. *NPJ Mater. Sustain.* **2026**, *4*, 11. [CrossRef]
164. Zhou, Y.; Wang, Z.; Tao, W.; Sun, Y.; Wu, J.; Wang, G.; Xiu, Y.; Ji, H.; Liu, Y.; Dong, A.; et al. Multi-objective optimization design of Al-Si alloys based on machine learning. *Calphad* **2025**, *90*, 102870. [CrossRef]
165. Zhu, S.; Sarıtürk, D.; Arróyave, R. Accelerating CALPHAD-based phase diagram predictions in complex alloys using universal machine learning potentials: Opportunities and challenges. *Acta Mater.* **2025**, *286*, 120747. [CrossRef]

Disclaimer/Publisher's Note: The statements, opinions and data contained in all publications are solely those of the individual author(s) and contributor(s) and not of MDPI and/or the editor(s). MDPI and/or the editor(s) disclaim responsibility for any injury to people or property resulting from any ideas, methods, instructions or products referred to in the content.